

¹ STANDARD MODEL IS BEST MODEL (WORKING TITLE)

² William Kennedy DiClemente

³ A DISSERTATION
⁴ in
⁵ Physics and Astronomy

⁶ Presented to the Faculties of The University of Pennsylvania
⁷ in Partial Fulfillment of the Requirements for the Degree of Doctor of Philosophy
⁸ 2019 Last compiled: January 16, 2019

⁹
¹⁰ I. Joseph Kroll, Professor, Physics
¹¹ Supervisor of Dissertation

¹²
¹³ Joshua Klein, Professor, Physics
¹⁴ Graduate Group Chairperson

¹⁵ Dissertation Committee
¹⁶ (Committee Prof. 1), Professor, Physics
¹⁷ (Committee Prof. 2), Associate Professor, Physics
¹⁸ (Committee Prof. 3), Professor, Physics
¹⁹ (Committee Prof. 4), Professor, Physics
²⁰ I. Joseph Kroll, Professor, Physics

21

S T A N D A R D M O D E L I S B E S T M O D E L (W O R K I N G T I T L E)

22
23
24

C O P Y R I G H T
2 0 1 9
William Kennedy DiClemente

25

All rights reserved.

Acknowledgements

27 I'd like to thanks the Ghosts of Penn Students Past for providing me with such an amazing thesis
28 template.

29

ABSTRACT

30

STANDARD MODEL IS BEST MODEL (WORKING TITLE)

31

William Kennedy DiClemente

32

J. Kroll

33

This is the abstract text.

Contents

35	Acknowledgements	iii
36	Abstract	iv
37	Contents	v
38	List of Tables	ix
39	List of Figures	xi
40	Preface	xiv
41	1 Introduction	1
42	2 Theoretical Framework	2
43	2.1 Introduction to the Standard Model	2
44	2.2 Electroweak Mixing and the Higgs Field	2
45	3 LHC and the ATLAS Detector	3
46	3.1 The Large Hadron Collider	3
47	3.2 The ATLAS Detector	3
48	3.2.1 The Inner Detector	3
49	3.2.1.1 Pixel Detector	3
50	3.2.1.2 Semiconductor Tracker	3
51	3.2.1.3 Transition Radiation Tracker	3
52	3.2.2 The Calorimeters	4

53	3.2.2.1	Liquid Argon Calorimeters	4
54	3.2.2.2	Tile Calorimeters	4
55	3.2.3	The Muon Spectrometer	4
56	3.2.4	Particle reconstruction	5
57	3.2.4.1	Track reconstruction	5
58	3.2.4.2	Muon reconstruction	5
59	3.2.4.3	Electron reconstruction	5
60	3.2.4.4	Jet reconstruction	5
61	4	Alignment of the ATLAS Inner Detector	6
62	4.1	Effects of Misalignment	6
63	4.2	The Alignment Method	6
64	4.3	Momentum Bias Corrections	6
65	4.4	Alignment of the IBL	7
66	4.5	Alignment Monitoring	7
67	5	Measurement of same-sign WW production at $\sqrt{s} = 13$ TeV with ATLAS	8
68	5.0.1	Theoretical overview of vector boson scattering	8
69	5.0.2	Same-sign $W^\pm W^\pm$ scattering	10
70	5.0.3	Overview of backgrounds	12
71	5.1	Data and Monte Carlo samples	14
72	5.1.1	Monte Carlo samples	14
73	5.2	Object and event selection	15
74	5.2.1	Object selection	15
75	5.2.1.1	Muon candidate selection	16
76	5.2.1.2	Electron candidate selection	18
77	5.2.1.3	Jet candidate selection	18
78	5.2.1.4	Treatment of overlapping objects	18
79	5.2.2	Signal event selection	20
80	5.3	Background estimations	22
81	5.3.1	Estimation of the WZ background	22
82	5.3.2	Estimation of the $V\gamma$ background	23
83	5.3.3	Estimation of backgrounds from charge misidentification	25

84	5.3.3.1	Validation of the charge misidentification estimate	28
85	5.3.4	Estimation of non-prompt backgrounds with the fake factor method	28
86	5.3.4.1	Overview of the default fake factor method	30
87	5.3.4.2	The fake factor with p_T^{cone}	31
88	5.3.4.3	Implementation of the fake factor	32
89	5.3.4.4	Results of the fake factor	33
90	5.3.4.5	Test of fake factor in validation regions	33
91	5.3.4.6	Systematic uncertainties	33
92	5.3.5	Reduction of WZ background using custom overlap removal	33
93	5.4	Cross section measurement	40
94	5.5	Results	40
95	6	Prospects for same-sign WW at the High Luminosity LHC	41
96	6.0.1	Analysis Overview	42
97	6.1	Theoretical motivation	42
98	6.1.1	Experimental sensitivity to longitudinal polarization	43
99	6.2	Monte Carlo samples	43
100	6.3	Background estimations	45
101	6.3.1	Truth-based isolation	46
102	6.4	Object and event selection	47
103	6.4.1	Object selection	47
104	6.4.2	Event selection	47
105	6.5	Selection optimization	48
106	6.5.1	Random grid search algorithm	48
107	6.5.2	Inputs to the optimization	51
108	6.5.3	Results of the optimization	52
109	6.6	Results	56
110	6.6.1	Event yields	56
111	6.6.2	Uncertainties	58
112	6.6.3	Cross section measurement	59
113	6.6.4	Longitudinal scattering significance	59
114	7	Conclusion	63

¹¹⁵	A Additional material on truth isolation	64
¹¹⁶	Bibliography	65

List of Tables

118	5.1	Predicted cross sections for EQK and QCD production of diboson processes relevant to VBS at $\sqrt{s} = 8\text{TeV}$ using the SHERPA MC generator. Loose generator level cuts are applied on lepton $p_T > 5\text{ GeV}$, dilepton invariant mass $m_{ll} > 4\text{ GeV}$, and at least two jets with $m_{jj} > 10\text{ GeV}$	11
119			
120	5.2	Summary of MC samples used in the analysis.	16
121			
122	5.3	Muon selection criteria. All muons are required to pass the preselection (top), and then either the signal (middle) or loose (bottom) criteria is applied to the preselected electrons.	17
123			
124	5.4	Electron selection criteria. All electrons are required to pass the preselection (top), and then either the signal (middle) or loose (bottom) criteria is applied to the preselected electrons.	19
125			
126	5.5	19
127			
128	5.6	Summary of the overlap removal procedure used in the analysis. If the criteria in the “check” column is met, in the “result” column, the object on the left of the arrow is removed in favor of the object on the right.	20
129			
130	5.7	Summary of trigger requirements for electrons and muons for $\sqrt{s} = 13\text{TeV}$ data collected in 2015 and 2016. At least one of the triggers must be satisfied.	21
131			
132	5.8	The signal event selection	22
133			
134	5.9	Event yields in the WZ control region before normalization. All lepton flavor channels are combined.	23
135			
136	5.10	Selection criteria for the $V\gamma$ control region.	25
137			
138	5.11	Event yields in the $V\gamma$ control region. The $V\gamma$ scale factor of 1.77 is calculated by scaling up the $Z\gamma$ and Z -jets backgrounds to account for the difference between the data and predicted total background.	25
139			
140	5.12	Selection criteria for the same-sign inclusive validation region.	28
141			
142	5.13	Custom OR definition. Leptons must pass this selection in order to be counted for the trilepton veto.	39
143			
144	6.1	Summary of MC samples used in the analysis.	45
145	6.2	Truth-based isolation requirements for electrons and muons.	46
146	6.3	Summary of the signal event selection.	48
147	6.4	Updates to the $W^\pm W^\pm jj$ event selection criteria after optimization. Cuts not listed remain unchanged from the default selection in Table 6.3.	52
148			

149	6.5	Signal and background event yields using the default event selection for an integrated luminosity of $\mathcal{L} = 3000 \text{ fb}^{-1}$. Events containing a fake or charge-flipped electron are removed from their respective sources and combined into a single entry each.	56
150	6.6	Signal and background event yields using the optimized event selection for an integrated luminosity of $\mathcal{L} = 3000 \text{ fb}^{-1}$. Events containing a fake or charge-flipped electron are removed from their respective sources and combined into a single entry each.	57
151	6.7	Summary of estimated experimental and rate uncertainties.	58
152	A.1	Event yields prior to applying any form of truth-based isolation criteria.	64
153	A.2	Event yields after applying a test version of the truth-based isolation.	64
154			
155			
156			
157			

List of Figures

159	3.1	General cut-away view of the ATLAS detector.	4
160	5.1	Cross sections in nanobarns for five different scattering processes of longitudinally polarized vector bosons as a function of center of mass energy \sqrt{s} . Without a SM Higgs boson (left), the cross sections grow unbounded with \sqrt{s} ; however with a 120 GeV Higgs boson (right), the cross sections no longer diverge.	9
161	5.2	Tree-level Feynman diagrams for VBS EWK $VVjj$ production including triple gauge couplings involving W and/or Z bosons (top left and top middle), quartic gauge coupling (top right), or the exchange of a Higgs boson (s -channel bottom left and t -channel bottom right). The labels are quarks (q), fermions (f), and gauge bosons ($V = W, Z$).	10
162	5.3	Tree-level Feynman diagrams for non-VBS EWK $VVjj$ production. The labels are quarks (q), fermions (f), and gauge bosons ($V = W, Z$).	10
163	5.4	Tree-level Feynman diagrams for QCD $VVjj$ production. The labels are quarks (q), fermions (f), and gauge bosons ($V = W, Z$).	11
164	5.5	Feynman diagrams for VBS EWK production of $W^\pm W^\pm jj$ events. The leftmost diagram contains a quartic gauge coupling vertex, and the rightmost diagram contains an exchange of a Higgs boson. TODO: Make diagrams consistent with others	12
165	5.6	$W^\pm W^\pm jj$ VBS event topology containing two leptons (1 and 2) with the same electric charge, two neutrinos, and two forward tagging jets (3 and 4) with large rapidity separation Δy .	12
166	5.7	Generator level comparisons at $\sqrt{s} = 8\text{TeV}$ of dijet invariant mass (m_{jj} , left) and dijet rapidity (Δy_{jj} , right) in EWK (red) and QCD (blue) $W^\pm W^\pm jj$ events. Both data sets have been normalized to the same area.	13
167	5.8	ATLAS event display of a $pp \rightarrow W^+W^+ \rightarrow \mu^+\nu_\mu\mu^+\nu_\mu jj$ event. The muons are represented by the red lines travelling from the ID through the MS, and the forward jets are represented by the blue cones with yellow energy deposits in the calorimeters. The direction of the E_T^{miss} in the transverse plane is indicated by the gray dashed line in the inset image. Event display taken from [1].	13
168	5.9	Leading lepton p_T (left) and η (right) distributions in the WZ control region before normalization. All lepton channels are combined.	24
169	5.10	Trilepton invariant mass m_{lll} distribution in the WZ control region before normalization. All lepton channels are combined.	24

190	5.11	Charge misidentification rates for electrons as a function of $ \eta $ and p_T . Rates are calculated from $Z \rightarrow e^+e^-$ MC after applying scale factors to approximate the charge mis-ID rates in data.	27
192	5.12	Dilepton invariant mass distribution m_{ll} for the ee channel in the same-sign inclusive VR.	29
193	5.13	p_T distributions for the leading (left) and subleading (right) electron for the ee channel in the same-sign inclusive VR. In these plots, the cut requiring m_{ee} to fall within the Z mass window has been inverted in order to test the modelling away from the Z peak.	29
197	5.14	Δp_T distributions for nominal (blue) and loose (red) muons in simulated $t\bar{t}$ events. Each muon has been matched to a truth-level jet within a cone of $\Delta R < 0.4$. Both distributions are normalized to unit area.	32
200	5.15	Graphical representation of the fake factor application using $p_T + p_T^{\text{cone}}$. The value of $p_T + p_T^{\text{cone}}$ for the loose lepton is used to “look up” the fake factor weight which is then applied to the event. The loose lepton’s p_T becomes $p_T + p_T^{\text{cone}}$ for the purpose of the fake background estimation.	33
205	5.16	The measured fake factor as a function of muon $p_T + p_T^{\text{cone}}$. The error bars represent the statistical uncertainty only.	34
206	5.17	The measured fake factor as a function of electron $p_T + p_T^{\text{cone}}$ in the central ($ \eta < 1.37$, blue) and forward ($ \eta > 1.37$, red) regions of the detector. The error bars represent the statistical uncertainty only.	34
209	5.18	Systematic variations in the fake factor as a function of muon $p_T + p_T^{\text{cone}}$. The individual fake factors obtained for each systematic variation are displayed with their statistical uncertainties.	35
212	5.19	Systematic variations in the fake factor as a function of electron $p_T + p_T^{\text{cone}}$ in the central ($ \eta < 1.37$, top) and forward ($ \eta > 1.37$, bottom) regions of the detector. The individual fake factors obtained for each systematic variation are displayed with their statistical uncertainties.	36
216	5.20	Pseudorapidity (η) distributions of truth muons (top) and electrons (bottom) for Sherpa $W^\pm W^\pm jj$ and WZ MC samples. The blue vertical lines represent the allowed η range for each lepton flavor. The numbers correspond to the number of raw MC events that fall within and outside of the allowed η range for each MC sample.	37
220	5.21	Distributions of $p_{T,\text{ratio}}(\mu, j)$ for EWK and QCD $W^\pm W^\pm jj$ signal (black) and WZ background (teal) for truth-matched third muons in events that pass the trilepton veto. Both distributions are normalized to unit area. The associated efficiency curves are on the right where efficiency is defined as the percentage of total events that would pass a cut on $p_{T,\text{ratio}}(\mu, j)$ at a given value on the x -axis.	37
225	5.22	Distributions of $\Delta R(\mu, j)$ for EWK and QCD $W^\pm W^\pm jj$ signal (black) and WZ background (teal) for truth-matched third muons in events that pass the trilepton veto. Both distributions are normalized to unit area. The associated efficiency curves are on the right where efficiency is defined as the percentage of total events that would pass a cut on $\Delta R(\mu, j)$ at a given value on the x -axis.	38
230	5.23	Distributions of $p_{T,\text{ratio}}(e, j)$ for EWK and QCD $W^\pm W^\pm jj$ signal (black) and WZ background (teal) for truth-matched third electrons in events that pass the trilepton veto. Both distributions are normalized to unit area. The associated efficiency curves are on the right where efficiency is defined as the percentage of total events that would pass a cut on $p_{T,\text{ratio}}(e, j)$ at a given value on the x -axis.	38
235	5.24	Two-dimensional plots of $p_{T,\text{ratio}}(\mu, j)$ vs $\Delta R(\mu, j)$ for truth-matched third muons in events that pass the trilepton veto for EWK and QCD $W^\pm W^\pm jj$ signal (left) and WZ background (right). The blue overlay indicates the area in which the third leptons will pass the custom OR and result in the event failing the trilepton veto.	39
238			

239	6.1	Comparison of the leading (top) and subleading (bottom) lepton p_T distributions for purely longitudinal (LL, black) and mixed polarization (LT+TT, cyan) $W^\pm W^\pm jj$ events.	44
240	6.2	Comparison of the azimuthal dijet separation ($ \Delta\phi_{jj} $) for purely longitudinal (LL, black) and mixed polarization (LT+TT, cyan) $W^\pm W^\pm jj$ events.	45
241	6.3	A visual representation of a rectangular grid search algorithm. The signal events are the blue triangles, and the red circles are the background events. TODO: replace with own figure	50
242	6.4	A visual representation of a random grid search algorithm. The signal events are the blue triangles, and the red circles are the background events. TODO: replace with own figure	50
243	6.5	Leading lepton p_T distribution. The default and optimized cuts are represented by the red and green dashed lines, respectively. The $W^\pm W^\pm jj$ EWK signal (black points) is normalized to the same area as the sum of the backgrounds (colored histogram). TODO: Move to appendix or omit	53
244	6.6	Dilepton invariant mass distribution. The default and optimized cuts are represented by the red and green dashed lines, respectively. The $W^\pm W^\pm jj$ EWK signal (black points) is normalized to the same area as the sum of the backgrounds (colored histogram). TODO: Move to appendix or omit	53
245	6.7	Leading (top) and subleading (bottom) jet p_T distributions. The default and optimized cuts are represented by the red and green dashed lines, respectively. The $W^\pm W^\pm jj$ EWK signal (black points) is normalized to the same area as the sum of the backgrounds (colored histogram).	54
246	6.8	Dijet invariant mass distribution. The default and optimized cuts are represented by the red and green dashed lines, respectively. The $W^\pm W^\pm jj$ EWK signal (black points) is normalized to the same area as the sum of the backgrounds (colored histogram). TODO: Move to appendix or omit	55
247	6.9	Lepton-jet centrality distribution. The default and optimized cuts are represented by the red and green dashed lines, respectively. The $W^\pm W^\pm jj$ EWK signal (black points) is normalized to the same area as the sum of the backgrounds (colored histogram).	55
248	6.10	p_T distributions for the leading jet using the default (left) and optimized (right) event selections for all channels combined.	57
249	6.11	p_T distributions for the subleading jet using the default (left) and optimized (right) event selections for all channels combined.	57
250	6.12	p_T distributions for lepton-jet centrality ζ using the default (left) and optimized (right) event selections for all channels combined.	58
251	6.13	Projections of the statistical (black), theoretical (blue), systematic (yellow), and total (red) uncertainties on the measured cross section as a function of integrated luminosity using the optimized event selection.	60
252	6.14	Dijet azimuthal separation ($ \Delta\phi_{jj} $) for the low m_{jj} region ($520 < m_{jj} < 1100$ GeV, top) and the high m_{jj} region ($m_{jj} > 1100$ GeV, bottom). The purely longitudinal (LL, gray) is plotted separately from the mixed and transverse (LT+TT, cyan) polarizations.	61
253	6.15	Projections of the expected longitudinal scattering significance as a function of integrated luminosity when considering all sources of uncertainties (black) or only statistical uncertainties (red).	62

283

Preface

²⁸⁴ This is the preface. It's optional, but it's nice to give some context for the reader and stuff.

285

Will K. DiClemente

Philadelphia, February 2019

286

CHAPTER 1

287

Introduction

288 The Standard Model (SM)¹ has been remarkably successful...

¹Here's a footnote.

289

CHAPTER 2

290

Theoretical Framework

291 (Some example introductory text for this chapter)...

292 2.1 Introduction to the Standard Model

293 Modern particle physics is generally interpreted in terms of the Standard Model (SM). This is a
294 quantum field theory which encapsulates our understanding of the electromagnetic, weak, and strong
295 interactions...

296 2.2 Electroweak Mixing and the Higgs Field

297 When the theory of the electroweak interaction was first developed [2, 3], the W and Z bosons were
298 predicted to be massless (a typical mass term in the Lagrangian would violate the $SU(2)$ symmetry).
299 However, these were experimentally observed to have masses...

300

CHAPTER 3

301

LHC and the ATLAS Detector

302

3.1 The Large Hadron Collider

303

The Large Hadron Collider (LHC) [4] is...

304

3.2 The ATLAS Detector

305

ATLAS is a general-purpose particle detector...

306

3.2.1 The Inner Detector

307

The Inner Detector serves the primary purpose of measuring the trajectories of charged particles...

308

3.2.1.1 Pixel Detector

309

The Pixel detector consists of four cylindrical barrel layers and three disk-shaped endcap layers...

310

3.2.1.2 Semiconductor Tracker

311

The Semiconductor Tracker uses the same basic technology as the Pixels, but the fundamental unit of silicon is a larger “strip”...

313

3.2.1.3 Transition Radiation Tracker

314

The Transition Radiation Tracker is the outermost component of the ID...

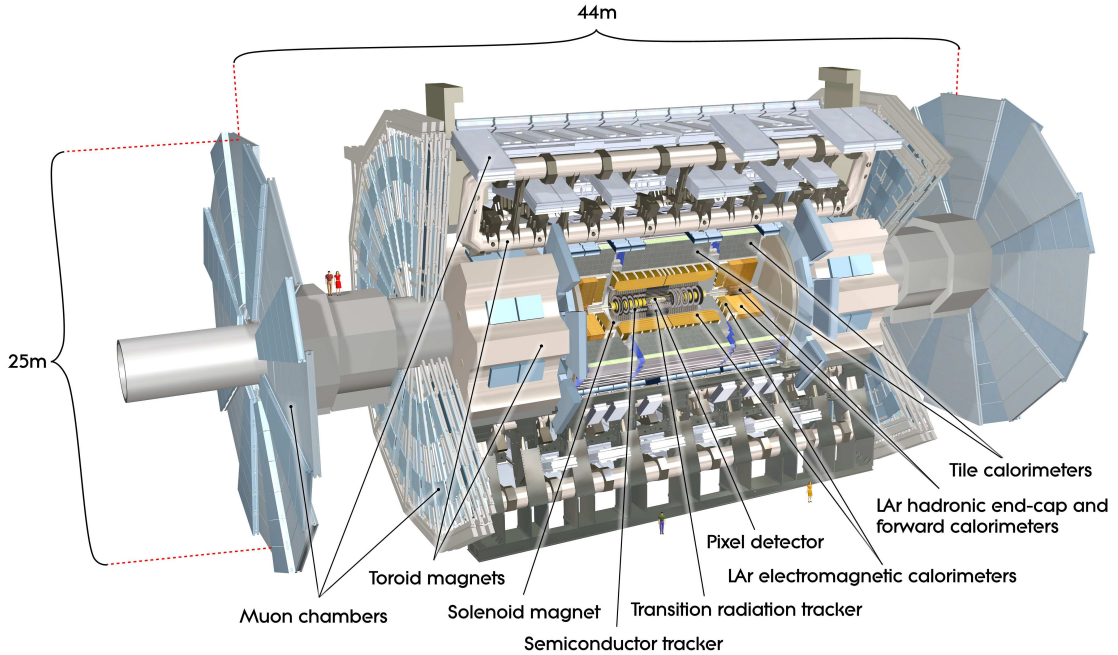


Figure 3.1: General cut-away view of the ATLAS detector [5].

3.2.2 The Calorimeters

ATLAS includes two types of calorimeter system for measuring electromagnetic and hadronic showers. These are the Liquid Argon (LAr) calorimeters and the Tile calorimeters. Together, these cover the region with $|\eta| < 4.9\dots$

3.2.2.1 Liquid Argon Calorimeters

The Liquid Argon system consists of...

3.2.2.2 Tile Calorimeters

The Tile calorimeter provides coverage for hadronic showers...

3.2.3 The Muon Spectrometer

Muon spectrometer stuff.

325 **3.2.4 Particle reconstruction**

326 Particle reconstruction algorithms

327 **3.2.4.1 Track reconstruction**

328 **3.2.4.2 Muon reconstruction**

329 **3.2.4.3 Electron reconstruction**

330 **3.2.4.4 Jet reconstruction**

CHAPTER 4

Alignment of the ATLAS Inner Detector

333 In order for the subdetectors of the ID to operate at their designed precisions, it is essential that
334 the locations of the sensors be known as precisely as possible. Differences between the expected and
335 actual positions of a sensor can result in displaced particle hits and degrade track reconstruction
336 quality. These misalignments can occur for any number of reasons, including but not limited to
337 elements shifting during maintenance periods or cycles in ATLAS's magnetic field, or simply small
338 movements during normal detector operations. Since it is not practical to physically realign hundreds
339 of thousands of detector elements to μm precision by hand, an iterative track-based alignment
340 algorithm is used to determine the physical positions and orientations of these elements [6]. The
341 effects of misalignments and the steps taken to correct and monitor them are detailed in this chapter.

342 4.1 Effects of Misalignment

343 Hello world!

344 4.2 The Alignment Method

345 Hello world!

346 4.3 Momentum Bias Corrections

347 Hello world!

³⁴⁸ **4.4 Alignment of the IBL**

³⁴⁹ Hello world!

³⁵⁰ **4.5 Alignment Monitoring**

³⁵¹ Hello world!

CHAPTER 5

Measurement of same-sign WW production at $\sqrt{s} = 13$ TeV with ATLAS

355 Production of same-sign W boson pairs is a particularly interesting SM process. When produced
 356 via vector boson scattering (VBS), $W^\pm W^\pm jj$ is particularly sensitive to the electroweak symmetry
 357 breaking (EWSB) mechanism as well as potential “beyond the Standard Model” (BSM) physics.
 358 $W^\pm W^\pm jj$ events can be produced via electroweak-mediated (EWK) diagrams, of which VBS is a
 359 subset, or QCD-mediated diagrams. The biggest advantage of same-sign $W^\pm W^\pm jj$ lies in its ratio
 360 of electroweak (EWK) to QCD production cross sections. Despite the opposite-sign $W^\pm W^\mp$ having
 361 a considerably larger total cross section, its EWK-mediated diagrams are considerably smaller than
 362 its QCD-mediated diagrams, while for same-sign $W^\pm W^\pm$ the ratio is approximately one to one.
 363 This makes $W^\pm W^\pm jj$ one of the best channels for studying VBS at the LHC.

364 The first evidence of electroweak (EWK) $W^\pm W^\pm jj$ production was seen by the ATLAS and CMS
 365 experiments at $\sqrt{s} = 8$ TeV with excesses of 3.6σ [7] and 2.0σ [8] over backgrounds, respectively. More
 366 recently, ATLAS and CMS have both observed the EWK process at $\sqrt{s} = 13$ TeV with significances
 367 of 6.9σ [1] and 5.5σ [9], respectively. The analysis presented in this chapter is based off of the ATLAS
 368 $\sqrt{s} = 13$ TeV observation and cross section measurement of EWK $W^\pm W^\pm jj$ production [1, 10].

369 5.0.1 Theoretical overview of vector boson scattering

370 VBS processes are very important to understand due to their sensitivity to the EWSB mechanism.
 371 The scattering amplitude of longitudinally polarized vector bosons grows with center-of-mass energy
 372 and ultimately violates unitarity above $\sqrt{s} = 1$ TeV in the absence of a light SM Higgs boson [11, 12].
 373 However, once the Higgs is introduced, the divergences cancel and the cross section no longer grows

374 unbounded, as can be seen in Figure 5.1, which consists of plots from [13].

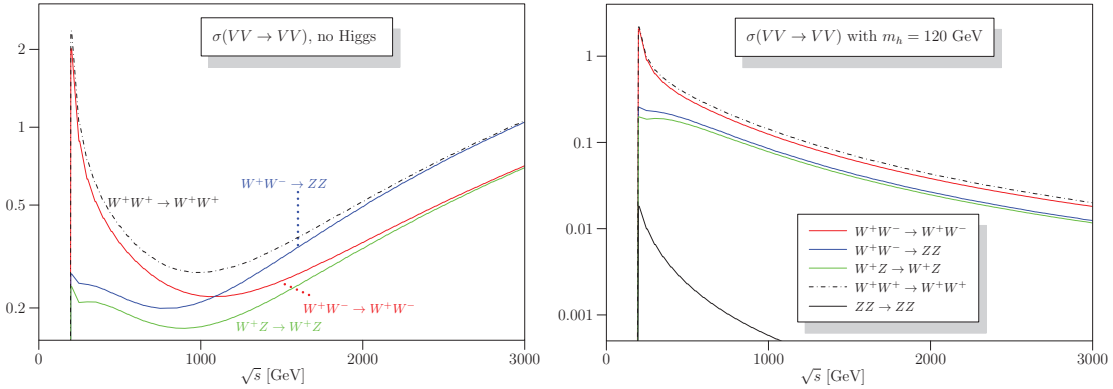


Figure 5.1: Cross sections in nanobarns for five different scattering processes of longitudinally polarized vector bosons as a function of center of mass energy \sqrt{s} . Without a SM Higgs boson (left), the cross sections grow unbounded with \sqrt{s} ; however with a 120 GeV Higgs boson (right), the cross sections no longer diverge. Plots taken from [13].

375 With the discovery of the Higgs boson in 2012 [14, 15], the EWSB mechanism can now be directly
376 studied. Due to the exchange of a Higgs in the s - and t -channel VBS diagrams ($W^\pm W^\pm jj$ itself only
377 contains the t -channel diagram), VBS processes are directly sensitive to properties of the Higgs. For
378 example, the high-mass tail in the VV scattering system allows an approximation of the effective
379 coupling strength of the Higgs to vector bosons that is independent of any assumptions on the Higgs
380 width [16]. Additionally, the center of mass energy dependence of the VV scattering can reveal
381 whether the Higgs boson unitarizes the longitudinal scattering amplitude fully or only partially [17].

382 VBS events are characterized by two quarks from the colliding protons each radiating a massive
383 vector boson which then scatter and decay in the detector. The incoming quarks carry a large
384 amount of momentum and only deflect a small amount upon radiating the vector boson; as a result,
385 they often travel very close to the beam line. Ignoring the decay products of the bosons, these VBS
386 events result in a final state of two vector bosons (V) and two jets (j) at high pseudorapidities
387 (called *forward jets*) from the outgoing quarks. The shorthand $VVjj$ is used to represent this final
388 state.

389 $VVjj$ events can be produced via two different physical processes. The first involves purely
390 electroweak interactions in the tree-level diagrams, with $\mathcal{O}(\alpha_{EWK}) = 6$ and will be referred to as
391 *EWK production*. This can be further broken down into VBS and non-VBS production. In the
392 VBS EWK production, the scattering occurs via triple or quartic gauge couplings, as well as the
393 s - or t -channel exchange of a Higgs boson. The non-VBS EWK production contains the same final

394 state of two vector bosons and two outgoing quarks, but the bosons do not scatter. Due to gauge
 395 invariance, it is not possible to separate the VBS from the non-VBS productions [18]; therefore,
 396 both are included in the signal generation and are indistinguishable from one another. The second
 397 process involves a mix of the EWK and strong interactions, of order $\mathcal{O}(\alpha_s) = 2 \otimes \mathcal{O}(\alpha_{EWK}) = 4$ and
 398 will be referred to as *QCD production*. The tree-level Feynman diagrams for VBS EWK, non-VBS
 399 EWK, and QCD $VVjj$ production are found in Figures 5.2, 5.3, and 5.4, respectively.

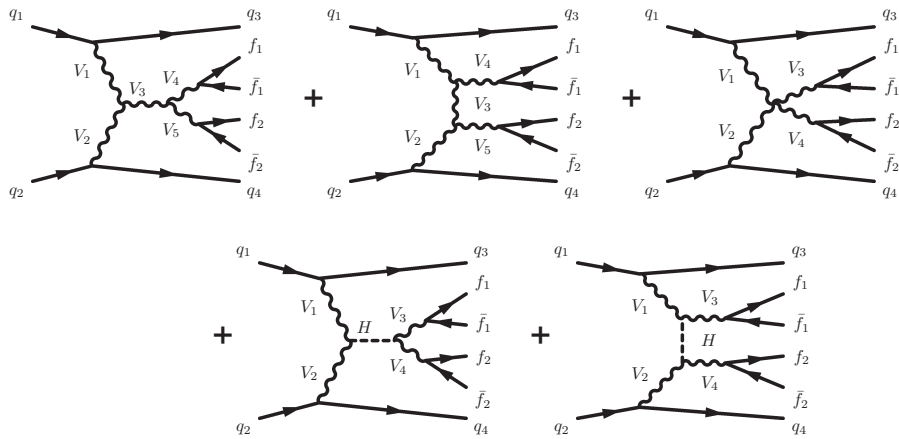


Figure 5.2: Tree-level Feynman diagrams for VBS EWK $VVjj$ production including triple gauge couplings involving W and/or Z bosons (top left and top middle), quartic gauge coupling (top right), or the exchange of a Higgs boson (s -channel bottom left and t -channel bottom right). The labels are quarks (q), fermions (f), and gauge bosons ($V = W, Z$).

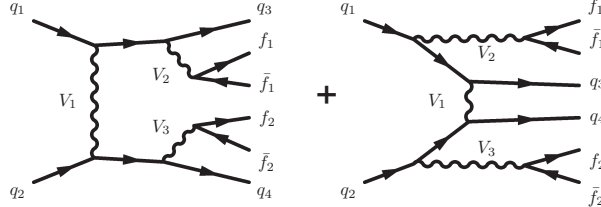


Figure 5.3: Tree-level Feynman diagrams for non-VBS EWK $VVjj$ production. The labels are quarks (q), fermions (f), and gauge bosons ($V = W, Z$).

400 5.0.2 Same-sign $W^\pm W^\pm$ scattering

401 Same-sign $W^\pm W^\pm jj$ scattering is considered to be one of the best channels for studying VBS at the
 402 LHC [16]. This is due primarily to the ratio of the EWK to the QCD production, which matters

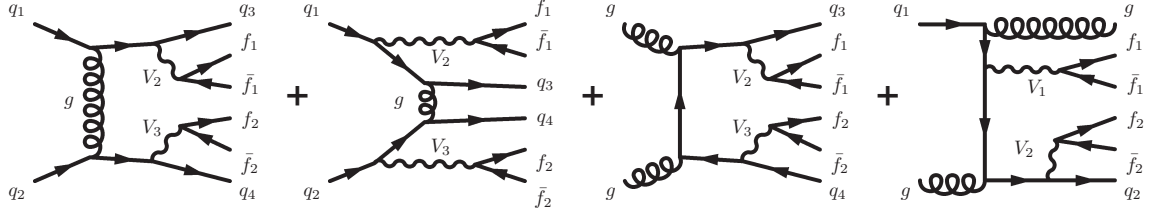


Figure 5.4: Tree-level Feynman diagrams for QCD $VVjj$ production. The labels are quarks (q), fermions (f), and gauge bosons ($V = W, Z$).

403 a great deal due to the VBS events being a subset of the total EWK production. In an analysis
 404 the EWK production would be considered the signal and the QCD production a background, so a
 405 favorable ratio of the two helps greatly when comparing the size of the signal to the backgrounds.
 406 A study at $\sqrt{s} = 8$ TeV [19] was done using the **SHERPA** Monte Carlo (MC) generator to calculate
 407 EWK and QCD production cross sections at leading order for a variety of $VVjj$ processes decaying
 408 to leptons and can be found in Table 5.1. Despite its lower cross section compared to other $VVjj$
 409 processes, the EWK to QCD ratio for $W^\pm W^\pm jj$ is approximately one-to-one, whereas for opposite-
 410 sign $W^\pm W^\mp jj$ the ratio is closer to 3%.

Process	Final state	σ_{EWK}	σ_{QCD}
$W^\pm W^\pm$	$l^\pm l^\pm \nu\nu jj$	19.5 fb	18.8 fb
$W^\pm W^\mp$	$l^\pm l^\mp \nu\nu jj$	91.3 fb	3030 fb
$W^\pm Z$	$l^\pm l^\pm l^\mp \nu jj$	30.2 fb	687 fb
ZZ	$l^+ l^- \nu\nu jj$	2.4 fb	162 fb
ZZ	$l^+ l^- l^+ l^- jj$	1.5 fb	106 fb

Table 5.1: Predicted cross sections for EQK and QCD production of diboson processes relevant to VBS at $\sqrt{s} = 8$ TeV using the **SHERPA** MC generator. Loose generator level cuts are applied on lepton $p_T > 5$ GeV, dilepton invariant mass $m_{ll} > 4$ GeV, and at least two jets with $m_{jj} > 10$ GeV. Numbers taken from [19].

411 This analysis studies $W^\pm W^\pm jj$ scattering where both W bosons decay leptonically to $e\nu$ or $\mu\nu$ ².
 412 The $W^\pm W^\pm jj$ VBS final state consists of two leptons with the same electric charge, two neutrinos,
 413 and two high energy forward jets with a large invariant mass. Tree-level Feynman diagrams of VBS
 414 $W^\pm W^\pm jj$ production can be found in Figure 5.5 and a visual representation of the VBS topology
 415 can be found in Figure 5.6. The two forward jets also serve as a powerful tool to suppress the
 416 QCD production mode. In EWK events, the two jets tend to have much higher separation and a

²Throughout the rest of this chapter, l denotes either electrons (e) or muons (μ) unless stated otherwise. Additionally, e , μ , and ν (neutrino) with no charge or anti-particle designation refer interchangeably to either the particle or anti-particle.

417 larger combined invariant mass than the two leading jets in a QCD event. The two plots shown in
 418 Figure 5.7 highlight the differences in these dijet quantities between the two production modes. An
 419 ATLAS event display of a real $W^\pm W^\pm jj$ candidate event is shown in Figure 5.8.

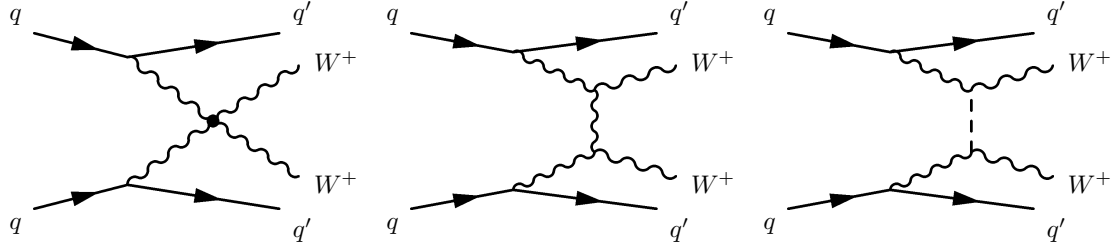


Figure 5.5: Feynman diagrams for VBS EWK production of $W^\pm W^\pm jj$ events. The leftmost diagram contains a quartic gauge coupling vertex, and the rightmost diagram contains an exchange of a Higgs boson. **TODO: Make diagrams consistent with others**

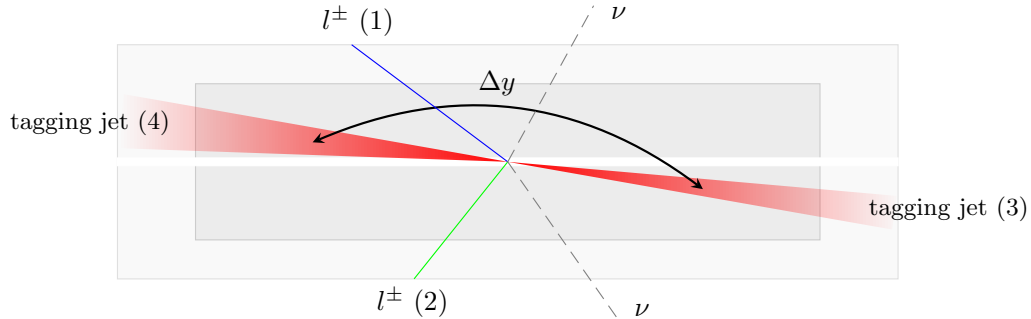


Figure 5.6: $W^\pm W^\pm jj$ VBS event topology containing two leptons (1 and 2) with the same electric charge, two neutrinos, and two forward tagging jets (3 and 4) with large rapidity separation Δy .

420 5.0.3 Overview of backgrounds

421 In addition to QCD production of $W^\pm W^\pm jj$ events, there are several other processes that can end
 422 up with a final state of two same-sign leptons, two neutrinos, and two jets. However, due to the ± 2
 423 final state charge, there is a considerable reduction in SM backgrounds (such as Z boson events)
 424 when compared to an analysis like opposite-sign $W^\pm W^\mp jj$.

425 One of the largest sources of background involves processes with prompt leptons³. These are

³Prompt leptons are those that are produced in the primary collision and are a direct decay product of the process

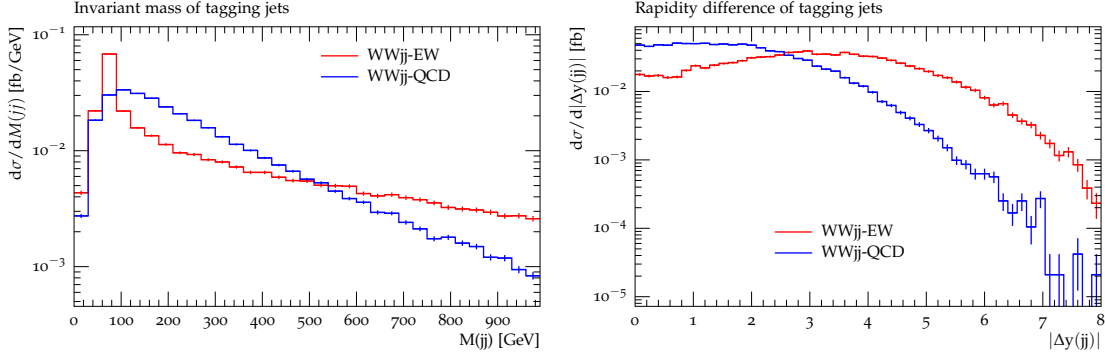


Figure 5.7: Generator level comparisons at $\sqrt{s} = 8$ TeV of dijet invariant mass (m_{jj} , left) and dijet rapidity (Δy_{jj} , right) in EWK (red) and QCD (blue) $W^{\pm}W^{\pm}jj$ events. Both data sets have been normalized to the same area. Plots taken from [19].

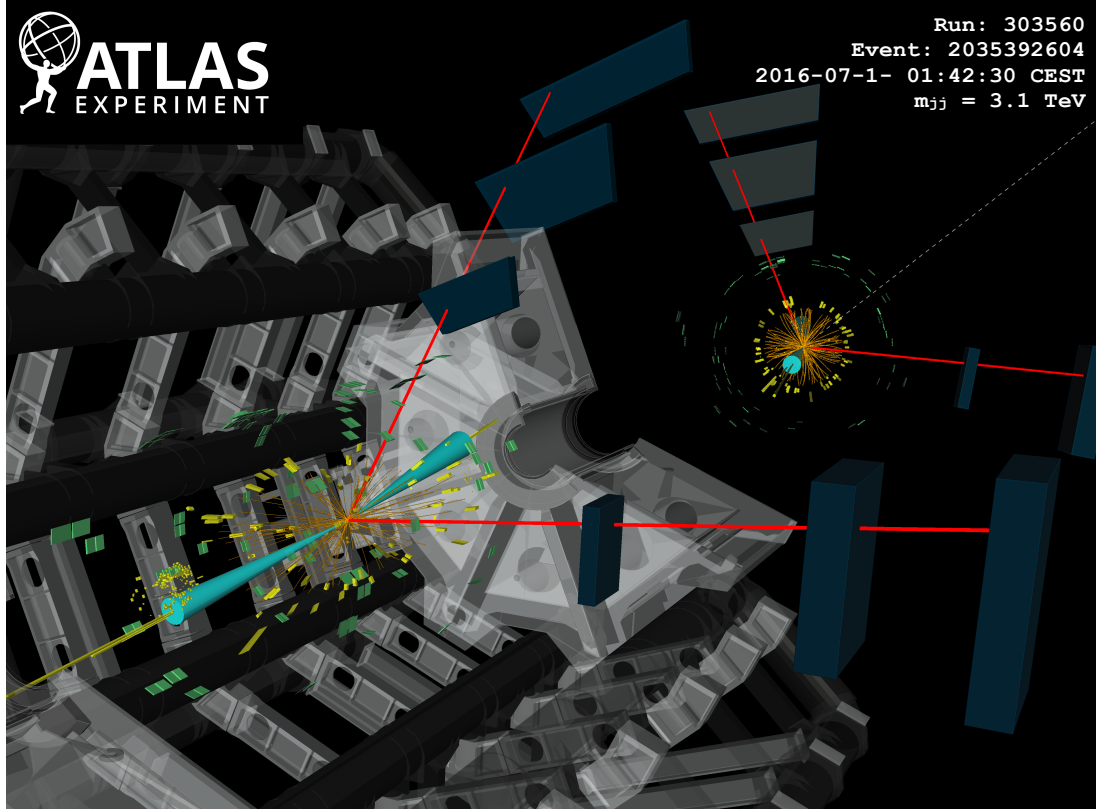


Figure 5.8: ATLAS event display of a $pp \rightarrow W^{\pm}W^{\pm} \rightarrow \mu^{\pm}\nu_{\mu}\mu^{\pm}\nu_{\mu}jj$ event. The muons are represented by the red lines travelling from the ID through the MS, and the forward jets are represented by the blue cones with yellow energy deposits in the calorimeters. The direction of the E_T^{miss} in the transverse plane is indicated by the gray dashed line in the inset image. Event display taken from [1].

426 events that contain two leptons with the same electric charge and one or more additional leptons
 427 that are “lost”, either by failing the selection criteria or falling outside of the detector’s acceptance.
 428 The number of processes that can contribute is limited by the requirement of same-sign leptons, and
 429 as a result this background is dominated by processes involving two or more vector bosons, with the
 430 largest contribution coming from WZ events and smaller contributions from ZZ and $t\bar{t}V$ events.
 431 Triboson events where one boson decays hadronically also contribute to this background; however,
 432 the jets are generally softer and more central than in a typical VBS event, and the cuts applied on
 433 the forward jets suppress these contributions.

434 The other dominant background comes from non-prompt, or “fake”, leptons. Here one or more
 435 leptons originate from the decay of another particle unrelated to the signal process, such as a
 436 heavy-flavor decay or photon conversion, or come from a jet that is misidentified as a lepton. This
 437 background is mostly made up of events from $t\bar{t}$ and $W+\text{jets}$ processes, with a much smaller contribu-
 438 tion from $V\gamma$ events. **TODO: check whether $V\gamma$ really qualifies as non-prompt, we lump $Z\gamma$ in**
 439 **with the charge flip background in the paper...**

440 Finally, opposite-sign lepton pairs can enter the signal region if one of the leptons is reconstructed
 441 with the wrong charge (called *charge misidentification*⁴). In practice, this only affects events with
 442 electrons, as the charge misidentification rate for muons is negligible [20]. This is a major background
 443 in events with two electrons, but is a much smaller contribution for events with one electron and
 444 one muon.

445 5.1 Data and Monte Carlo samples

446 This analysis uses 36.1 fb^{-1} of $\sqrt{s} = 13$ TeV proton-proton collision data recorded by ATLAS
 447 during 2015 and 2016. The uncertainty in the combined integrated luminosity is 2.1%. It is derived
 448 following a methodology similar to that detailed in [21] and using the LUCID-2 detector for the
 449 baseline luminosity measurements [22] from calibration of the luminosity scale using x - y beam-
 450 separation scans.

451 5.1.1 Monte Carlo samples

452 A number of Monte Carlo (MC) simulations are employed to model signal and background pro-
 453 cesses. In order to model the real collision data as closely as possible, each MC has been run through

of interest. Non-prompt leptons originate from some secondary process, such as a b -hadron decay, or are jets that get mis-reconstructed as a lepton.

⁴Charge misidentification is also referred to interchangeably as *charge mis-ID* and *charge flip*.

454 a full simulation of the ATLAS detector [23] in GEANT4 [24], and events have been reconstructed
 455 using the same algorithms as the data. The simulation reproduces as closely as possible the momen-
 456 tum resolutions and calorimeter responses of the detector, and also includes the effects of pileup by
 457 including soft QCD interactions using PYTHIA v8.1 [25]. The MC samples used in this analysis are
 458 detailed in this section and summarized in Table 5.2.

459 The $W^\pm W^\pm jj$ samples are modeled using SHERPA v2.2.2 [26, 27, 28] with the NNPDF3.0 PDF
 460 set [29]. The EWK signal samples are generated by fixing the electroweak coupling constant to
 461 $\mathcal{O}(\alpha_W) = 6$, and a QCD background sample was also generated with $\mathcal{O}(\alpha_W) = 4$. SHERPA includes
 462 up to one parton at next-to-leading order (NLO) and up to three at leading order (LO) in the
 463 strong coupling constant α_s . A second $W^\pm W^\pm jj$ EWK sample is generated using POWHEG-BOX
 464 v2 [30] with the NNPDF3.0 PDF set and at NLO accuracy. This sample is only used for systematic
 465 studies, as POWHEG-BOX does not include resonant triboson contributions in its matrix element, which
 466 are non-negligible at NLO [31].

467 Diboson processes (VV where $V = W, Z$) are simulated with SHERPA v2.2.2 for mixed hadronic
 468 and leptonic decays and SHERPA v2.2.1 for fully leptonic decays of the bosons. Similarly, triboson
 469 (VVV) and $V\gamma$ processes are simulated using SHERPA v2.1.1 with up to one parton at NLO and up
 470 to three at LO. $W+jets$ processes are simulated with SHERPA2.2.1 with up to two partons at NLO
 471 and four at LO. All the above SHERPA samples use the NNPDF3.0 PDF set and SHERPA's own parton
 472 showering. The $Z+jets$ events are generated with Madgraph5_aMC@NLO [32] at LO and interfaced
 473 with PYTHIA v8.1 for parton showering.

474 $t\bar{t}$ events are generated using POWHEG-BOX v2 with the CT10 PDF set [33]. $t\bar{t}V$ samples are
 475 generated at NLO with Madgraph5_aMC@NLO and the NNPDF3.0 PDF set interfaced with PYTHIA v8
 476 for parton showering. Finally, single top events are generated with POWHEG-BOX v1 and the CT10f4
 477 PDF set interfaced with PYTHIA v6 [34] for parton showering.

478 5.2 Object and event selection

479 This section details the selection criteria for objects used in the analysis as well as the selection for
 480 signal events.

481 5.2.1 Object selection

482 Muons, electrons, and jets all must pass strict selection requirements to ensure that only high quality,
 483 well measured objects are used. For leptons, a baseline selection is defined (called the *preselection*),

Process	Generator	Comments
$W^\pm W^\pm jj$ (EWK)	SHERPA v2.2.2	Signal sample
$W^\pm W^\pm jj$ (EWK)	POWHEG-BOX v2	Systematics sample
$W^\pm W^\pm jj$ (QCD)	SHERPA v2.2.2	
Diboson	SHERPA v2.2.2	Both bosons decay leptonically ($llll$, $lll\nu$, $ll\nu\nu$)
Triboson	SHERPA v2.2.1	One boson decays leptonically, the other hadronically
$V\gamma$	SHERPA v2.1.1	
$V\gamma jj$ (EWK)	SHERPA v2.2.4	
$t\bar{t}V$	Madgraph5_aMC@NLO	
$t\bar{t}$	POWHEG-BOX v2	
Single top	POWHEG-BOX v1	EWK t -, s -, & Wt -channels

Table 5.2: Summary of MC samples used in the analysis.

484 which all leptons must pass in order to be considered for the analysis. This preselection is an
 485 intentionally loose set of criteria in order to have high acceptance for rejecting backgrounds with
 486 additional leptons (i.e. $WZ \rightarrow 3l\nu jj$). Signal leptons are then required to satisfy a much tighter
 487 *signal selection* aimed at suppressing backgrounds from non-prompt or fake leptons. A third set of
 488 lepton selection criteria, the *loose selection*, defines a sample enriched in non-prompt leptons, and
 489 it is used in the fake factor method for estimating the non-prompt background, discussed in detail
 490 in Section 5.3.4. Jets are only required to pass one set of selection criteria. These selections are
 491 detailed in the following sections and summarized in Table 5.3 for muons, Table 5.4 for electrons,
 492 and Table 5.5 for jets.

493 5.2.1.1 Muon candidate selection

494 Cuts on muon p_T serve to reject low momentum leptons from background processes and additional
 495 collisions from pileup events. Preselected muons must have $p_T > 6$ GeV and signal muons $p_T >$
 496 27 GeV. The p_T requirement for loose muons is lower than for signal muons, $p_T > 15$ GeV, for
 497 reasons that are discussed in Section 5.3.4. **TODO:** reference proper subsection when it's done
 498 Muons are required to fall within the detector's η acceptance: $|\eta| < 2.7$ for preselected muons,
 499 which is tightened to $|\eta| < 2.5$ for the signal muons.

500 Cuts on the transverse and longitudinal impact parameters are applied to ensure that the can-
 501 didate muon originated from the primary particle interaction and not some other source, such as a
 502 heavy flavor decay. The preselection and the loose selection both have looser requirements on the
 503 transverse impact parameter significance (d_0/σ_{d_0}) than the signal selection; all three have the same

504 requirement on the transverse impact parameter ($|z_0 \times \sin \theta|$).

505 Finally, the muon candidates are required to pass a particle identification and an isolation criteria
 506 as defined in [35]. The methods used in constructing the identification and isolation workingpoints
 507 are described in more detail in Section 3.2.4.2. The muon identification serves to select prompt muons
 508 with high efficiency and well measured momenta. This analysis uses two different workingpoints,
 509 **Loose** for preselected muons and **Medium** for loose and signal muons, where **Medium** muons are a
 510 tighter subset of those that pass the **Loose** requirement. Muon isolation is a measurement of detector
 511 activity around the muon candidate, and it is measured with both track-based and calorimeter-
 512 based variables. The isolation workingpoint used for the signal muons, **Gradient**, is defined such
 513 that there is 90% or better background rejection efficiency for 25 GeV muons, and 99% efficiency at
 514 60 GeV. There is no minimum isolation requirement for preselected or loose muons. Loose muons
 515 are additionally required to fail one or both of the signal transverse impact parameter cut and signal
 516 isolation requirement.

Muon preselection	
Momentum cut	$p_T > 6$ GeV
Angular acceptance	$ \eta < 2.7$
Longitudinal impact parameter	$ z_0 \times \sin \theta < 0.5$ mm
Transverse impact parameter	$d_0/\sigma_{d_0} < 10$
Particle identification	Loose

Muon signal selection	
Momentum cut	$p_T > 27$ GeV
Angular acceptance	$ \eta < 2.5$
Longitudinal impact parameter	$ z_0 \times \sin \theta < 0.5$ mm
Transverse impact parameter	$d_0/\sigma_{d_0} < 3$
Particle identification	Medium
Particle isolation	Gradient

Muon loose selection	
Momentum cut	$p_T > 15$ GeV
Angular acceptance	$ \eta < 2.5$
Longitudinal impact parameter	$ z_0 \times \sin \theta < 0.5$ mm
Transverse impact parameter	$d_0/\sigma_{d_0} < 10$
Particle identification	Medium
Fail signal transverse impact parameter and/or isolation cuts	

Table 5.3: Muon selection criteria. All muons are required to pass the preselection (top), and then either the signal (middle) or loose (bottom) criteria is applied to the preselected electrons.

517 **5.2.1.2 Electron candidate selection**

518 The electron candidate selections are very similar to those for muons. The p_T cut starts at $p_T >$
 519 6 GeV for the preselection, increases to $p_T > 20$ GeV for loose electrons, and finally to $p_T > 27$ GeV
 520 for signal electrons. The $|\eta|$ cut for electrons requires $|\eta| < 2.47$ for all electrons, with the region
 521 $1.37 \leq |\eta| \leq 1.52$ removed from loose and signal electrons. This region is where the electromagnetic
 522 calorimeter transitions from the barrel to the endcaps and is not fully instrumented. Both the
 523 transverse and longitudinal impact parameter cuts are the same for all electron selections.

524 The electron particle identification uses a multivariate likelihood technique (LH) [36] detailed
 525 in Section 3.2.4.3. Preselected electrons must pass the loosest LH workingpoint `LooseLH` with
 526 an additional requirement that there be a reconstructed track hit in the first layer of the pixel
 527 detector (a so-called *B*-layer hit). The LH requirement for the loose and signal electrons the tightness
 528 of the identification using `MediumLH` and `TightLH`, respectively. As for isolation, the `Gradient`
 529 workingpoint is required for signal electrons only. The loose electrons must fail one or both of the
 530 signal identification and isolation requirements.

531 **5.2.1.3 Jet candidate selection**

532 The final objects that need to pass selection are jets. Jets are clustered using the anti- k_t algo-
 533 rithm [37] within a radius of $\Delta R = 0.4$. The jets are then calibrated using E_T - and η -dependent
 534 correction factors that are trained using MC simulations [38]. These calibrated jets are then re-
 535 quired to have $p_T > 30$ GeV if they lie in the forward regions of the detector ($2.4 < |\eta| < 4.5$) and
 536 $p_T > 25$ GeV in the central region ($|\eta| \leq 2.4$). In order to suppress pileup jets, the so-called jet-
 537 vertex-tagger (JVT) discriminant associates a jet with the primary interaction vertex [39]; central
 538 jets with $p_T > 60$ GeV are required to pass the `Medium` JVT workingpoint, which corresponds to
 539 an average efficiency of over 92%. Finally, the jets are required to be separated by selected prompt
 540 leptons by at least $\Delta R(j, l) > 0.3$.

541 **5.2.1.4 Treatment of overlapping objects**

542 In the event that one or more objects are reconstructed very close to each other, there is the
 543 possibility for double-counting if both originated from the same object. The procedure by which
 544 this ambiguity is resolved is called *overlap removal* (OR). The standard ATLAS recommendation
 545 for OR is implemented in this analysis [40, 41] and is summarized in Table 5.6.

Electron preselection	
Momentum cut	$p_T > 6$ GeV
Angular acceptance	$ \eta < 2.47$
Longitudinal impact parameter	$ z_0 \times \sin \theta < 0.5$ mm
Transverse impact parameter	$d_0/\sigma_{d_0} < 5$
Particle identification	LooseLH + B-layer hit

Electron signal selection	
Momentum cut	$p_T > 27$ GeV
Angular acceptance	$ \eta < 2.47$, excluding $1.37 \leq \eta \leq 1.52$
Longitudinal impact parameter	$ z_0 \times \sin \theta < 0.5$ mm
Transverse impact parameter	$d_0/\sigma_{d_0} < 5$
Particle identification	TightLH
Particle isolation	Gradient

Electron loose selection	
Momentum cut	$p_T > 20$ GeV
Angular acceptance	$ \eta < 2.47$, excluding $1.37 \leq \eta \leq 1.52$
Longitudinal impact parameter	$ z_0 \times \sin \theta < 0.5$ mm
Transverse impact parameter	$d_0/\sigma_{d_0} < 5$
Particle identification	MediumLH
Fail signal identification and/or isolation cuts	

Table 5.4: Electron selection criteria. All electrons are required to pass the preselection (top), and then either the signal (middle) or loose (bottom) criteria is applied to the preselected electrons.

Jet selection	
Momentum cut	$p_T > 30$ GeV for $2.4 < \eta < 4.5$ $p_T > 60$ GeV for $ \eta < 2.4$
JVT cut	Medium
Jet-lepton separation	$\Delta R(j, l) > 0.3$

Table 5.5:

546 Since electrons leave a shower in the EM calorimeter, every electron has a jet associated with
 547 it. Therefore, any jets close to an electron (within $\Delta R(e, j) < 0.2$) are rejected due to the high
 548 probability that they are the same object. On the other hand, when jets and electrons overlap
 549 within a large radius of $0.2 < \Delta R(e, j) < 0.4$, it is likely that the electron and jet both are part of
 550 a heavy-flavor decay, and the electron is rejected.

551 High energy muons can produce photons via bremsstrahlung radiation or collinear final state
 552 radiation which results in a nearby energy deposit in the calorimeters. Non-prompt muons from
 553 hadronic decays produce a similar signature; however, in this case the jet has a higher track multiplicity
 554 in the ID. It is possible to address both cases by rejecting the jet when the ID track multiplicity
 555 is less than three and otherwise rejecting the muon for jets and muons within $\Delta R(\mu, j) < 0.4$.

556 In addition to the case above where muon bremsstrahlung results in a nearby reconstructed jet,
 557 the ID track from the muon and the calorimeter energy deposit can lead to it being reconstructed
 558 as an electron. In this case, if both a muon and an electron share a track in the ID, the muon is
 559 kept and the electron is rejected, unless the muon is calorimeter-tagged⁵, in which case the muon is
 560 removed in favor of the electron.

Overlap	Check	Result (remove → keep)
Electron & Jet	$\Delta R(e, j) < 0.2$	Jet → electron
	$0.2 < \Delta R(e, j) < 0.4$	Electron → jet
Muon & Jet	$\Delta R(\mu, j) < 0.4$ and Jet N_{ID} tracks < 3	Jet → muon
	$\Delta R(\mu, j) < 0.4$ and Jet N_{ID} tracks ≥ 3	Muon → jet
Electron & Muon	Shared ID track	Electron → muon
	Shared ID track & muon is calo-tagged	Muon → electron

Table 5.6: Summary of the overlap removal procedure used in the analysis. If the criteria in the “check” column is met, in the “result” column, the object on the left of the arrow is removed in favor of the object on the right.

561 5.2.2 Signal event selection

562 After the objects have been selected, cuts are applied on a per-event level to select $W^\pm W^\pm jj$ signal
 563 events. The event selection is summarized in Table 5.8 and is detailed in this section. It includes
 564 the results of an optimization performed using a multidimensional grid scan.

565 The initial event selection begins by choosing events that pass one or more of the trigger re-
 566 quirements listed in Table 5.7. At least one signal lepton is “matched” to a passed trigger in order

⁵A calorimeter-tagged (CT) muon is a muon that is identified by matching an ID track to a calorimeter energy deposit. CT muons have relatively low reconstruction efficiency compared to those measured by the MS, but can be used to recover acceptance in regions of the detector where the MS does not have full coverage [35].

567 to ensure that it was indeed a signal lepton that fired the trigger. A collection of *event cleaning*
 568 cuts must also be passed in order to remove events collected during periods in which one or more
 569 components of the detector was not operating optimally. Finally, the events are required to contain
 570 at least one interaction vertex. An event can have multiple reconstructed vertices from additional
 571 proton-proton collisions that occurred in the same bunch crossing. In this case, the *primary vertex*
 572 is determined by choosing the vertex with the largest sum of the p_T^2 of its associated tracks.

	2015 data	2016 data
Electrons	$p_T > 24$ GeV and Medium ID	$p_T > 26$ GeV and Tight ID and Loose isolation
	$p_T > 60$ GeV and Medium ID	$p_T > 60$ GeV and Medium ID
	$p_T > 120$ GeV and Loose ID	$p_T > 140$ GeV and Loose ID
Muons	$p_T > 20$ GeV and Loose isolation $p_T > 50$ GeV	$p_T > 26$ GeV and Medium isolation $p_T > 50$ GeV

Table 5.7: Summary of trigger requirements for electrons and muons for $\sqrt{s} = 13$ TeV data collected in 2015 and 2016. At least one of the triggers must be satisfied.

573 Events are then required to contain exactly two signal leptons with the same electric charge.
 574 The dilepton pair must have a combined invariant mass of $m_{ll} \geq 20$ GeV in order to suppress low
 575 mass Drell-Yan backgrounds. Two additional selections are applied to events in the ee-channel:
 576 both electrons are required to have $|\eta| < 1.37$ with an invariant mass at least 15 GeV away from
 577 the Z -boson mass to reduce events where one electron is reconstructed with the wrong charge (this
 578 background will be discussed in more detail in Section 5.3 TODO: Replace with proper subsection
 579 once it's written). To suppress backgrounds from events with more than two leptons, events with
 580 more than two leptons passing the preselection are vetoed.

581 Missing transverse energy (E_T^{miss}) represents any particles that escape the detector without
 582 being measured, such as neutrinos, and is defined as the magnitude of the vector sum of transverse
 583 momenta of all reconstructed objects. It can be difficult to calculate accurately, as it involves
 584 measurements from all subsystems within the detector, and it is sensitive to any corrections that
 585 may be applied to the reconstructed physics objects [42]. These corrections, including the momentum
 586 smearing for muons, energy scale and smearing for electrons, and jet calibrations, are propagated
 587 to the E_T^{miss} calculation. Events are required to contain $E_T^{\text{miss}} > 30$ GeV in order to account for the
 588 two neutrinos from the W boson decays.

589 At least two jets are required. The leading and subleading jets must have $p_T > 65$ GeV and
 590 $p_T > 35$ GeV, respectively, and are referred to as the *tagging jets*. Events are vetoed if they contain
 591 one or more jets that have been tagged as a b -jet to suppress backgrounds from heavy flavor decays

592 (especially top quark events). The b -tagging algorithm used by ATLAS is a boosted decision tree
 593 (BDT) called MV2c10, and this analysis uses a workingpoint with 85% efficiency [43].

594 Finally, cuts are applied on the VBS signature outlined in Section 5.0.2. The tagging jets are
 595 required to have a dijet invariant mass $m_{jj} > 200$ GeV and be separated in rapidity by $|\Delta y_{jj}| > 2.0$.
 596 This preferentially selects the VBS EWK events over the QCD-produced $W^\pm W^\pm jj$ events.

Event selection	
Event preselection	Pass at least one trigger with a matched lepton Pass event cleaning At least one reconstructed vertex
Lepton selection	Exactly two leptons passing signal selection Both signal leptons with the same electric charge $ \eta < 1.37$ and $ M_{ee} - M_Z > 15$ GeV (ee -channel only) Veto events with more than two preselected leptons
Missing transverse energy	$E_T^{\text{miss}} \geq 30$ GeV
Jet selection	At least two jets Leading jet $p_T > 65$ GeV Subleading jet $p_T > 35$ GeV $m_{jj} > 200$ GeV $N_{b\text{-jet}} = 0$ $ \Delta y_{jj} > 2.0$

Table 5.8: The signal event selection

597 5.3 Background estimations

598 The major sources of background events are summarized in Section 5.0.3, and the methods used to
 599 estimate them are detailed in this section. Prompt backgrounds from ZZ and $t\bar{t}V$ are estimated
 600 directly from MC simulations. The shape of the WZ and $V\gamma$ backgrounds are taken from MC, and
 601 the predicted yeilds are normalized to the data predictions in dedicated control regions, as outlined
 602 in Sections 5.3.1 and 5.3.2, respectively. Opposite sign events with a charge misidentified electron
 603 are estimated by a data-driven background method which is summarized in Section 5.3.3. Finally, a
 604 *fake factor* method is used to estimate the contributions from non-prompt backgrounds and is the
 605 subject of Section 5.3.4.

606 5.3.1 Estimation of the WZ background

607 The dominant background involving prompt leptons comes from $WZ + \text{jets}$ events. The contribution
 608 is estimated from MC simulation and normalized to data in a control region enriched in WZ events

609 defined by the same event selection as Table 5.8 for the signal region, with the following changes
 610 applied to increase the purity of the WZ process:

- 611 • The third lepton veto is inverted, requiring a third lepton with $p_T > 15$ GeV
- 612 • Two of the leptons must make a same-flavor opposite-sign pair. If more than one pair exists,
 613 the one with m_{ll} closest to the Z boson mass is chosen.
- 614 • The trilepton invariant mass is required to be $m_{lll} > 106$ GeV to reduce contributions from
 615 $Z\gamma$ and $Z+jets$

616 Once the event yields in the control region are calculated, they are propagated to the final
 617 signal region fit, detailed in Section 5.4 TODO: update reference with proper subsection once it's
 618 written, in a single bin combining all the lepton channels. The systematic uncertainties of the WZ
 619 background are also calculated at this time. The event yields for the WZ control region are listed
 620 in Table 5.9, and distributions of the leading lepton p_T and η as well as trilepton invariant mass
 621 m_{lll} are found in Figures 5.10 and 5.9, respectively.

Event yields in the WZ control region	
WZ	197.9 ± 1.4
ZZ	14.1 ± 0.3
Triboson	1.26 ± 0.1
top	10.8 ± 1.1
$Z\gamma$	3.1 ± 1.1
$Z+jets$	2.5 ± 1.4
Total prediction	229.7 ± 2.5
Data	201 ± 14.2

Table 5.9: Event yields in the WZ control region before normalization. All lepton flavor channels are combined.

622 5.3.2 Estimation of the $V\gamma$ background

623 Events from $V\gamma$ processes can pass selection if the photon converts into an e^+e^- pair and one of the
 624 electrons passes the selection criteria. The background is estimated from MC simulations which are
 625 then scaled by a normalization factor calculated from a control region enriched in $Z(\mu^+\mu^-)\gamma$ events.
 626 This control region selects two opposite-sign muons and an additional electron that is assumed to
 627 come from the photon conversion. The full event selection is detailed in Table 5.10.

628 The $Z\gamma$ MC samples available do not cover the full range of p_T^γ and $\Delta R(\gamma, l)$; thus, additional
 629 Drell-Yan samples ($Z+jets$) are used to fill out the phase space. Overlap between the two samples

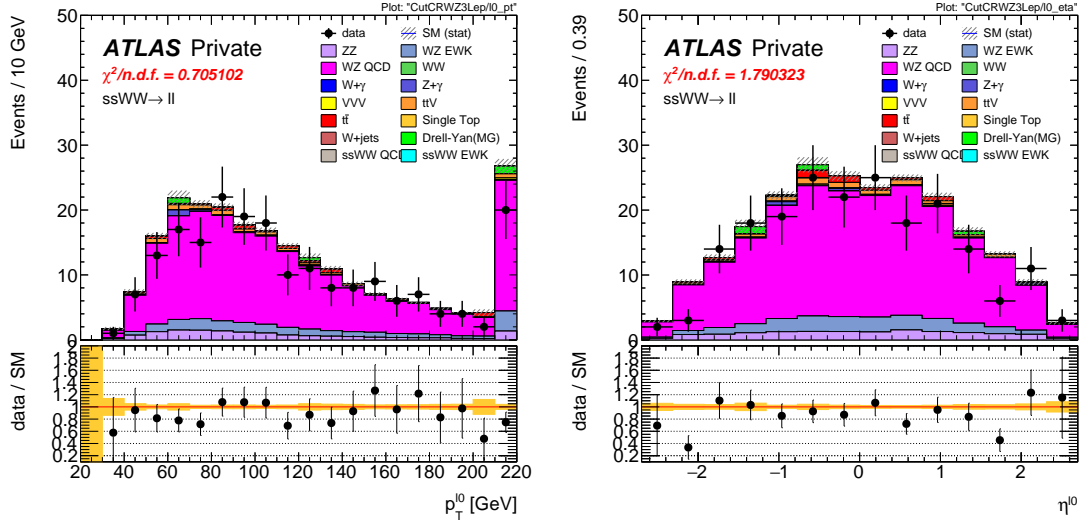


Figure 5.9: Leading lepton p_T (left) and η (right) distributions in the WZ control region before normalization. All lepton channels are combined.

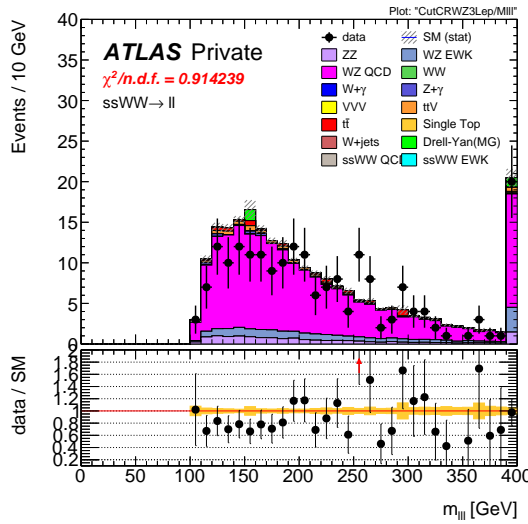


Figure 5.10: Trilepton invariant mass m_{lll} distribution in the WZ control region before normalization. All lepton channels are combined.

$V\gamma$ control region
Exactly two muons with $p_T > 27$ GeV and $p_T > 20$ GeV
Exactly one additional electron with $p_T > 15$ GeV
Remove overlap between $Z+jets$ and $Z\gamma$
Di-muon + photon invariant mass $75 < M_{\mu\mu\gamma} < 100$ GeV
$E_T^{\text{miss}} < 30$ GeV

Table 5.10: Selection criteria for the $V\gamma$ control region.

630 are removed based to avoid double counting. Events with final state photons at truth level are
 631 checked to ensure that the photon did not originate from a hadronic decay. Cuts on $p_T^\gamma > 10$ GeV
 632 and $\Delta R(\gamma, l) > 0.1$ are then applied at generator level, and $Z\gamma$ events that fail and $Z+jets$ events
 633 that pass this additional selection are removed.

634 The normalization factor is calculated directly from the event yields in the $V\gamma$ control region
 635 rather than in the signal fit, as is done for the WZ background. The event yields are listed in
 636 Table 5.11, and the normalization factor is determined to be 1.77. No MC events from $Z\gamma$ processes
 637 survive the full event selection; thus, the scaling is only applied to the $W\gamma$ background in the signal
 638 region. A systematic uncertainty of 44% is assigned to the background based off of the uncertainties
 639 in the calculation of the normalization factor.

Event yields in the $V\gamma$ control region	
$Z\gamma$	24.6 ± 3.3
$Z+jets$	3.0 ± 1.5
diboson + triboson	6.7 ± 0.3
top	1.5 ± 0.5
Total prediction	35.8 ± 3.7
Data	57 ± 7.6

Table 5.11: Event yields in the $V\gamma$ control region. The $V\gamma$ scale factor of 1.77 is calculated by scaling up the $Z\gamma$ and $Z+jets$ backgrounds to account for the difference between the data and predicted total background.

640 5.3.3 Estimation of backgrounds from charge misidentification

641 If an electron's charge is mis-reconstructed, it can lead to a real, opposite-sign lepton pair passing
 642 the same-sign requirement in the event selection. There are two primary reasons this can occur:
 643 1. An electron emits a photon via bremsstrahlung which then converts into an electron-positron
 644 pair, and the conversion track with the wrong electric charge is matched to the original electron.

645 This is the dominant process leading to charge flip, and it is highly dependent on the electron
 646 η due to the different amount of detector material the electron passes through.

647 2. The curvature of the electron’s track is mismeasured, resulting in the wrong charge being
 648 assigned. This process is dependent on the momentum of the electron, as its track becomes
 649 more straight as the momentum of the electron increases.

650 In order to estimate this background, the rate at which an electron’s charge is misidentified is
 651 calculated from $Z \rightarrow e^+e^-$ MC simulation. It is known that the MC does not perfectly model
 652 the material effects leading to charge flip; as a result, scale factors are applied to the MC in order
 653 for it to better reflect the real performance. These scale factors are obtained from the ratio of
 654 charge mis-ID rates in data and uncorrected MC in [10] following the method outlined in [44]. Once
 655 the scale factors are applied, the charge misidentification rate ε can be extracted by comparing the
 656 electron’s reconstructed charge with the charge of its truth particle:

$$\varepsilon(\eta, p_T) = \frac{N_{\text{wrong charge}}}{N_{\text{prompt electrons}}} \quad (5.1)$$

657 The charge mis-ID rate is calculated in bins of electron $|\eta|$ and p_T and varies from below 0.1% in the
 658 central region of the detector up to 8% in the forward regions for high p_T (above 90 GeV) electrons.
 659 A two-dimensional plot of ε can be found in Figure 5.11.

660 Given the charge flip rate $\varepsilon(\eta, p_T)$, the rate at which an electron has its charge correctly recon-
 661 structed is $(1 - \varepsilon)$. Thus there are three possible combinations of charge identification, assuming a
 662 two-electron event:

663 1. Both electrons are reconstructed correctly: $(1 - \varepsilon)^2$

664 2. Both electrons are mis-reconstructed: ε^2

665 3. Only one electron is mis-reconstructed: $2\varepsilon(1 - \varepsilon)$

666 In order to estimate the size of the background from charge misidentification, opposite-sign events
 667 are selected using the default event selection for a given signal or control region with the same-sign
 668 requirement inverted. These events are then weighted by the probability for one of the electrons to
 669 be reconstructed with the wrong charge:

$$\omega = \frac{\varepsilon_1(1 - \varepsilon_2) + \varepsilon_2(1 - \varepsilon_1)}{(1 - \varepsilon_1)(1 - \varepsilon_2) + \varepsilon_1\varepsilon_2} \quad (5.2)$$

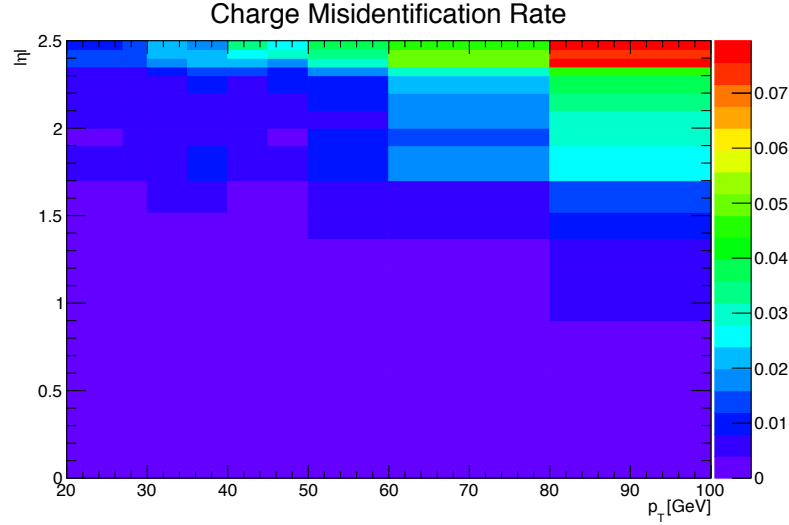


Figure 5.11: Charge misidentification rates for electrons as a function of $|\eta|$ and p_T . Rates are calculated from $Z \rightarrow e^+ e^-$ MC after applying scale factors to approximate the charge mis-ID rates in data.

670 where the subscripts 1 and 2 refer to the leading and subleading electrons, respectively, and ε_i is a
 671 function of the η and p_T of the i^{th} electron. In the case of an event with only one electron and one
 672 muon, Equation 5.2 simplifies:

$$\omega = \frac{\varepsilon}{1 - \varepsilon} \quad (5.3)$$

673 This method assumes that there is little contamination from fake electrons in the opposite-sign
 674 sample, and this has been verified with MC simulation.

675 Additionally, charge-flipped electrons tend to be reconstructed with lower energy when compared
 676 to electrons with the correct charge. This is due to energy loss from the material interactions that
 677 can cause the charge to be misidentified. A correction factor is calculated from MC simulations,
 678 comparing the p_T of the truth electron to its reconstructed counterpart:

$$\alpha = \frac{\left(\frac{p_T^{\text{reco}}}{p_T^{\text{truth}}} - 1 \right)_{\text{correct charge}}}{\left(\frac{p_T^{\text{reco}}}{p_T^{\text{truth}}} - 1 \right)_{\text{wrong charge}}} \quad (5.4)$$

679 The correction is then applied to the p_T of the charge-flipped electron via

$$p_T = p_T^0 / (1 + \alpha) + dE \quad (5.5)$$

680 where p_T^0 is the uncorrected p_T of the electron and dE is a gaussian smearing factor centered at
 681 zero with a width related to the energy resolution. Since which electron is misreconstructed is never

682 determined in this method, in the case of a two-electron event, the energy correction is applied
 683 randomly to one of the two electrons based on the probabilities for them to be charge-flipped. This
 684 also determines the overall sign of the event; the charge of the electron that does not receive the
 685 correction is taken to be the charge for both.

686 Systematic uncertainties on the charge mis-ID rates are calculated by generating two additional
 687 sets of rates with the uncertainties on the scale factors varied up and down. The size of the esti-
 688 mated charge flip background without the energy correction applied is also taken as a systematic
 689 uncertainty. These systematic uncertainties are estimated to be approximately $\pm 15\%$.

690 5.3.3.1 Validation of the charge misidentification estimate

691 The performance of the charge misidentification estimation is tested in the same-sign inclusive
 692 validation region (VR), defined in Table 5.12. For ee events, the mass of the dilepton pair is required
 693 to lie within 15 GeV of the Z boson mass to increase the purity of the charge flip background.
 694 $t\bar{t}$ production, which can contribute to both the charge mis-ID and fake lepton backgrounds, is
 695 suppressed by the b -jet veto. The di-electron invariant mass is shown in Figure 5.12, and distributions
 696 of the leading and subleading electron p_T in the ee -channel are shown in Figure 5.13 with the Z
 697 mass cut inverted. Agreement between data and prediction is seen within the total statistical and
 698 systematic uncertainties in the VR.

Same-sign inclusive VR
Exactly 2 same-sign signal leptons
$p_T > 27$ GeV for both leptons
$m_{ll} > 20$ GeV
$ m_{ee} - m_Z > 15$ GeV (ee -channel only)
$N_{b\text{-jet}} = 0$

Table 5.12: Selection criteria for the same-sign inclusive validation region.

699 5.3.4 Estimation of non-prompt backgrounds with the fake factor method

700 Events with one prompt lepton produced in association with hadronic jets can pass the event selection
 701 if a jet is misidentified as a charged lepton or if a non-prompt lepton from the decay of a heavy
 702 flavor particle (such as b - and c -hadrons) passes the signal lepton criteria. These misidentified jets
 703 and non-prompt leptons are collectively referred to as *fake leptons*, or simply *fakes*. The rate at
 704 which a fake lepton is misidentified is generally not modelled well enough by the MC to accurately
 705 estimate their contributions directly from simulation. Therefore, a data-driven technique called the

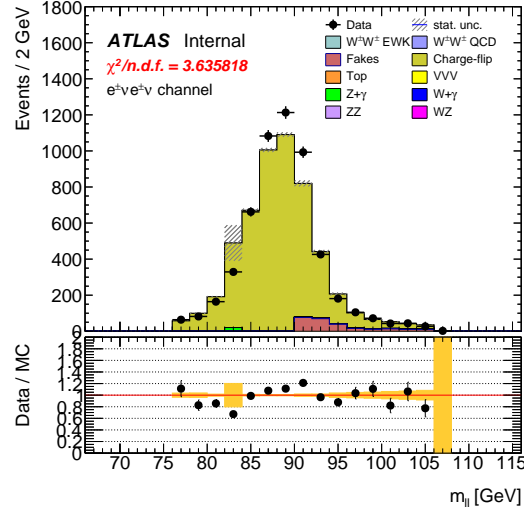


Figure 5.12: Dilepton invariant mass distribution m_{ll} for the ee channel in the same-sign inclusive VR.

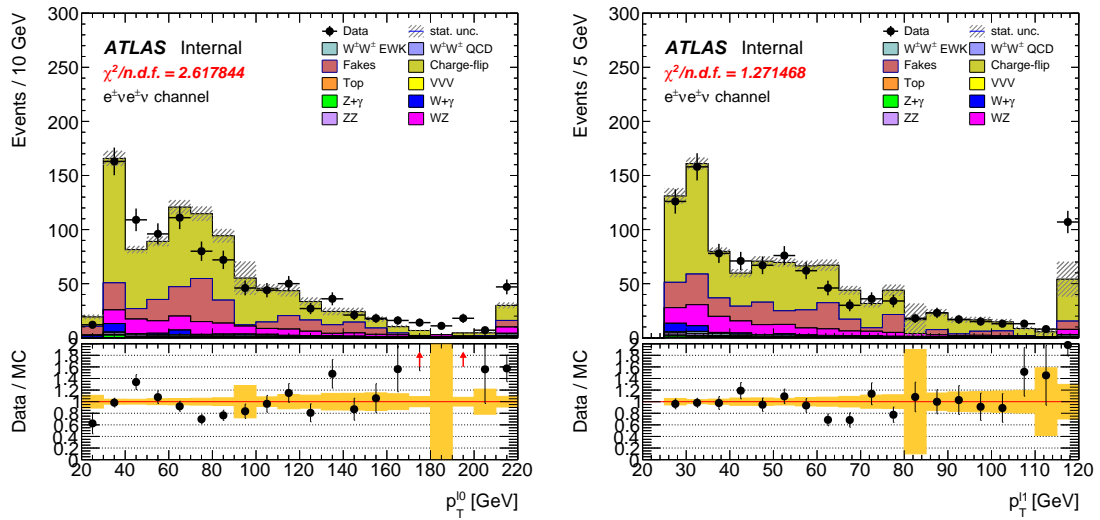


Figure 5.13: p_T distributions for the leading (left) and subleading (right) electron for the ee channel in the same-sign inclusive VR. In these plots, the cut requiring m_{ee} to fall within the Z mass window has been inverted in order to test the modelling away from the Z peak.

706 *fake factor* is used to estimate the size and shape of background processes from fake leptons. In this
 707 analysis, a new modification to the fake factor is used involving the particle isolation variables; the
 708 method is outlined in the context of the *default* fake factor in Section 5.3.4.1, and the modified fake
 709 factor is outlined in Section 5.3.4.2.

710 **5.3.4.1 Overview of the default fake factor method**

711 The goal of the fake factor method is to measure the fake rate in a region enriched in fake leptons
 712 and use it to estimate the size of the fake lepton background in a chosen signal or control region.
 713 This is done by creating two samples of leptons:

- 714 1. The *nominal* sample is made up of leptons passing the signal selection.
 715 2. The *loose* sample is made up of leptons that fail the signal selection while still passing a
 716 loosened set of criteria. This sample is enriched in fake leptons and is orthogonal to the set of
 717 signal leptons.

718 Using the sets of nominal and loose leptons, a fake factor f can be calculated in a region enriched
 719 in processes that are prone to producing fake leptons:

$$f = \frac{N_{\text{nominal}}}{N_{\text{loose}}} \quad (5.6)$$

720 Since the fake rate is not expected to be constant over the entire phase space, the fake factor can
 721 be divided into bins in a chosen quantity:

$$f(b) = \frac{N_{\text{nominal}}(b)}{N_{\text{loose}}(b)} \quad (5.7)$$

722 where b represents the bin number.

723 In order to estimate the fake background contribution in a given signal or control region, the
 724 fake factor is applied to a second control region with a selection identical to the region of interest
 725 with one of the leptons required to satisfy the loose criteria. The region for which the background
 726 is estimated contains two nominal leptons and is referred to as *nominal+nominal* (*NN*), and the
 727 associated control region where the fake factor is applied contains one nominal and one loose lepton
 728 and is referred to as *nominal+loose* (*NL*). The fake background in a *NN* region can then be
 729 calculated as:

$$N_{NN}^{\text{fake bkg.}} = \sum_b f(b) N_{NL}(b) \quad (5.8)$$

730 Backgrounds containing two prompt leptons can also enter the NL region if one of the leptons
 731 passes the nominal selection and the other passes the loose selection. Since the fake factor method
 732 estimates the fake background by scaling the amount of non-prompt events in the NL region, if these
 733 prompt contributions are not removed, they will be included in the scaling and the background
 734 will be overpredicted. The final estimate of the fake background becomes:

$$N_{NN}^{\text{fake bkg.}} = \sum_b f(b) (N_{NL}(b) - N_{NL}^{\text{prompt}}(b)) \quad (5.9)$$

735 **5.3.4.2 The fake factor with p_T^{cone}**

736 When a jet produces a non-prompt lepton, that lepton only carries a fraction of the underlying jet's
 737 total momentum. Due to the isolation cut applied to the nominal leptons, they typically carry a
 738 much larger percentage of the underlying jet momentum⁶ than the loose leptons (which are allowed
 739 to fail this criteria).

740 This discrepancy in the underlying jet momentum fraction can cause problems in the calculation
 741 of the fake factor f . Consider the case where two separate events have jets of identical momentum,
 742 but one produces a non-prompt lepton that passes the nominal selection, and the other produces a
 743 non-prompt lepton that passes the loose selection. The loose lepton on average will have lower p_T
 744 than the nominal lepton despite both originating from jets with the same momentum. This can be
 745 seen explicitly when comparing the p_T of a muon to its associated jet:

$$\Delta p_T(\mu, j) = \frac{p_T(j) - p_T(\mu)}{p_T(j) + p_T(\mu)} \quad (5.10)$$

746 Since muons are not included in the jet reconstruction algorithm, Δp_T approximates the momentum
 747 of the muon compared to the rest of the jet. For muons that carry more than 50% of the jet's
 748 momentum, Δp_T will be negative and vice-versa. The Δp_T distributions for nominal and loose
 749 muons in $t\bar{t}$ MC events is shown Figure 5.14, where a 50 GeV jet on average corresponds to a
 750 35 GeV nominal muon and a 20 GeV loose muon⁷.

751 Since the default fake factor defined in Equation 5.7 is typically binned in lepton p_T , within
 752 a given bin, the underlying jet p_T spectrum can differ substantially between the numerator and
 753 the denominator. Additionally, these differences can vary depending on the process producing the

⁶Since the isolation variables are a measure of detector activity around the lepton, if other nearby particles carried a significant portion of the jet's momentum, the lepton would likely fail this cut.

⁷To better illustrate the point, here the muon is added back into the jet p_T , and the corresponding muon p_T is obtained via $\Delta p_T(\mu, j) = \frac{(p_T(j) - p_T\mu) - p_T(\mu)}{(p_T(j) - p_T\mu) + p_T(\mu)} = \frac{p_T(j) - 2p_T(\mu)}{p_T(j)}$.

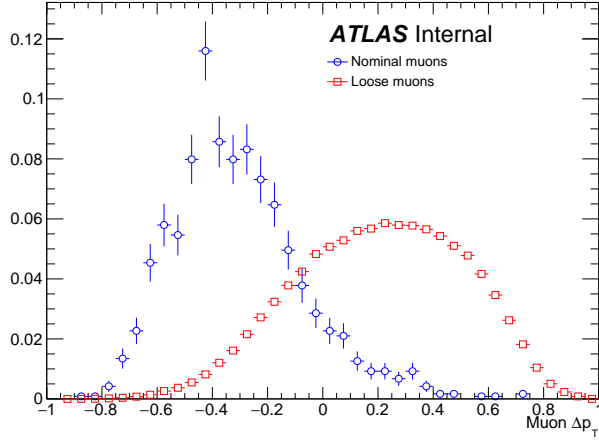


Figure 5.14: Δp_T distributions for nominal (blue) and loose (red) muons in simulated $t\bar{t}$ events. Each muon has been matched to a truth-level jet within a cone of $\Delta R < 0.4$. Both distributions are normalized to unit area.

754 non-prompt leptons or on the specific kinematic selections of the signal or control regions where the
 755 fake factor is applied.

756 Fortunately, the majority of the jet momentum not carried by the non-prompt lepton (excluding
 757 neutrinos) can be recovered using isolation variables. A track-based isolation is chosen, referred to
 758 as p_T^{cone} , and it contains the sum of the p_T of all particle tracks originating from the primary vertex
 759 within a cone of $\Delta R < 0.3$ around the lepton. **TODO: Start here tomorrow – finish up adding the**
 760 **$p_T + p_T^{\text{cone}}$ denominator explanation, add the dpt plots and one showing that p_T^{cone} is negligible for**
 761 **numerator etc** Thus, the denominator of the fake factor is binned in $p_T + p_T^{\text{cone}}$ is chosen to represent
 762 the loose lepton

$$f_b = \frac{N_{\text{nominal}}^{b(p_T)}}{N_{\text{loose}}^{b(p_T + p_T^{\text{cone}})}} \quad (5.11)$$

763 5.3.4.3 Implementation of the fake factor

764 The fake factor itself is measured from a sample of dijet events containing exactly one lepton and one
 765 b -jet that is approximately back-to-back with the lepton. This b -jet requirement serves to enhance
 766 non-prompt lepton contributions while suppressing contributions from processes involving W and
 767 Z bosons.

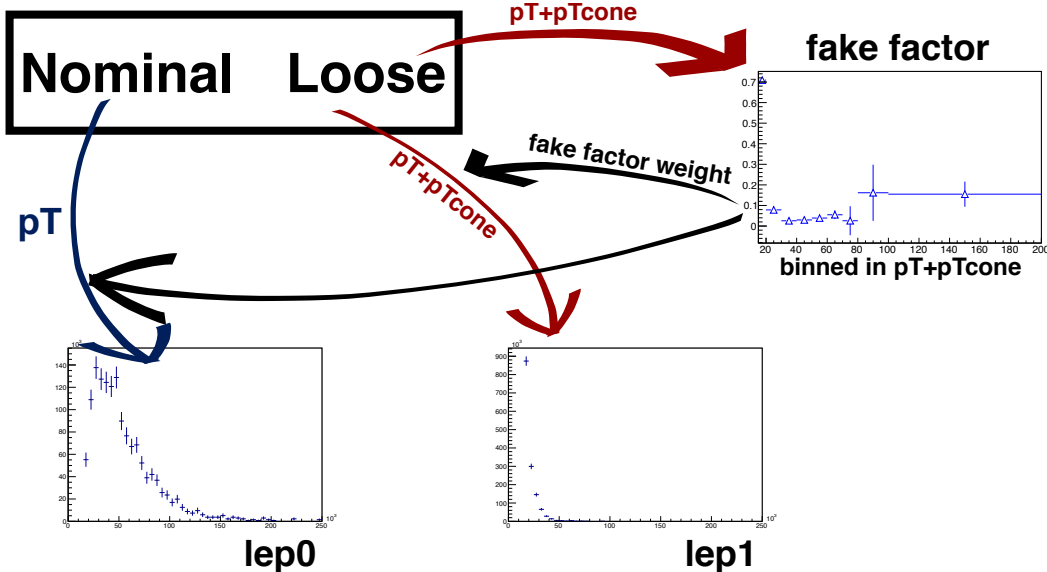


Figure 5.15: Graphical representation of the fake factor application using $p_T + p_{T\text{cone}}^{\text{cone}}$. The value of $p_T + p_{T\text{cone}}^{\text{cone}}$ for the loose lepton is used to “look up” the fake factor weight which is then applied to the event. The loose lepton’s p_T becomes $p_T + p_{T\text{cone}}^{\text{cone}}$ for the purpose of the fake background estimation.

768 5.3.4.4 Results of the fake factor

769 5.3.4.5 Test of fake factor in validation regions

770 5.3.4.6 Systematic uncertainties

771 5.3.5 Reduction of WZ background using custom overlap removal

772 The dominant source of prompt background in this analysis comes from WZ events where both
 773 bosons decay leptonically. Traditionally, the background is dealt with by imposing a veto on any
 774 event with a third lepton passing some loose identification criteria (the so-called *trilepton veto*). In
 775 the case of this analysis, if one or more leptons (in addition to the two signal leptons) passed the
 776 preselection criteria, the event would be rejected. However, WZ events can still enter the signal
 777 region if one of the leptons fails the veto selection or falls outside of the detector’s acceptance.

778 In order to understand the sources of WZ events that are not removed by the trilepton veto, a
 779 study was performed on truth-level leptons⁸ on $W^\pm W^\pm jj$ and WZ MC samples. Events with three
 780 truth leptons were selected, and each was matched to its reconstruction-level partner by finding

⁸Truth particles are the particles produced directly by the MC generator before being passed through the full detector simulation, at which point they are considered *reconstruction-level* (or *reco-level*) particles.

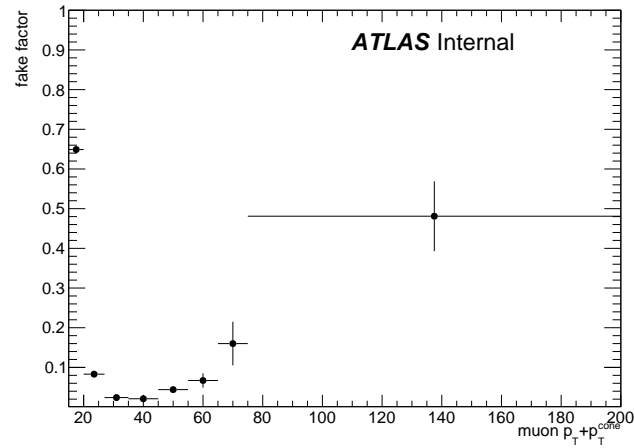


Figure 5.16: The measured fake factor as a function of muon $p_T + p_T^{\text{cone}}$. The error bars represent the statistical uncertainty only.

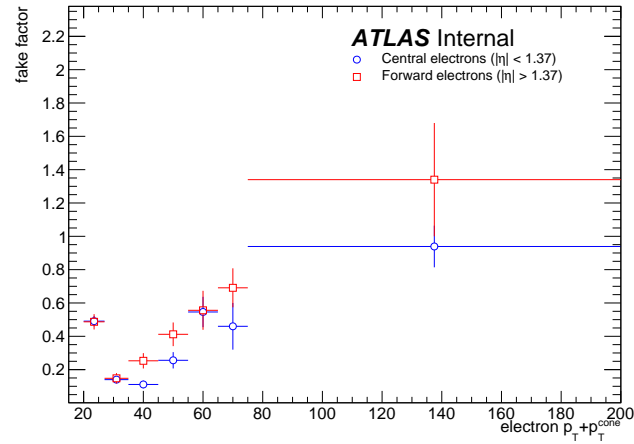


Figure 5.17: The measured fake factor as a function of electron $p_T + p_T^{\text{cone}}$ in the central ($|\eta| < 1.37$, blue) and forward ($|\eta| > 1.37$, red) regions of the detector. The error bars represent the statistical uncertainty only.

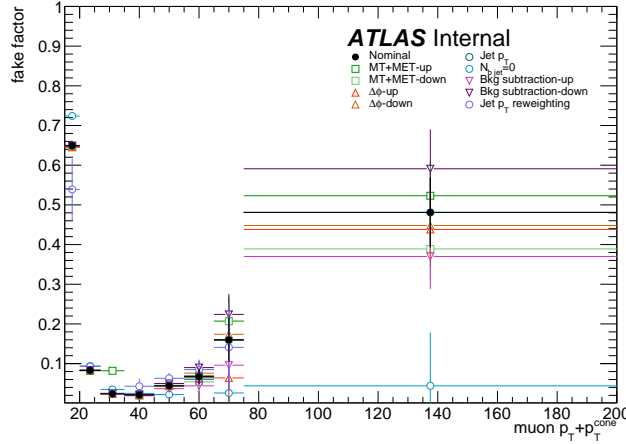


Figure 5.18: Systematic variations in the fake factor as a function of muon $p_T + p_T^{\text{cone}}$. The individual fake factors obtained for each systematic variation are displayed with their statistical uncertainties.

the closest $\Delta R(\text{truth}, \text{reco})$ and $\Delta p_{T,\text{truth,reco}}$ match. For events surviving the trilepton veto, the two signal leptons were removed, and the remaining leptons represent real leptons that failed to be selected for the veto. Between 40-50% of these leptons fell outside of the eta acceptance of the analysis (see Figure 5.20) and were unrecoverable. The second largest source of leptons failing the preselection was the OR, defined in Section 5.2.1.4. The standard OF procedure appeared to be too aggressive in removing leptons in favor of jets, causing many three lepton events to “lose” their third lepton and pass the trilepton veto. Therefore a *Custom OR* was investigated which would replace the standard OR in the preselection and allow for better WZ rejection by removing fewer third leptons.

TODO: Mention how the extra leptons in the $W^\pm W^\pm jj$ are background leptons since there are only 2 from the main decay

In order to construct a “custom” OR, a new quantity is defined between a lepton (l) and a nearby jet (j)

$$p_{T,\text{ratio}}(l, j) = \frac{p_{Tl}}{p_{Tj}} \quad (5.12)$$

which, along with $\Delta R(l, j)$, will allow for more third leptons to pass the preselection. The idea behind including $p_{T,\text{ratio}}$ is to be able to preferentially remove background leptons originating from jets (i.e. those that carry a low percentage of the total jet momentum) instead of removing *any* lepton near to jet. The distributions of $p_{T,\text{ratio}}$ and the associated efficiency curves for muons and

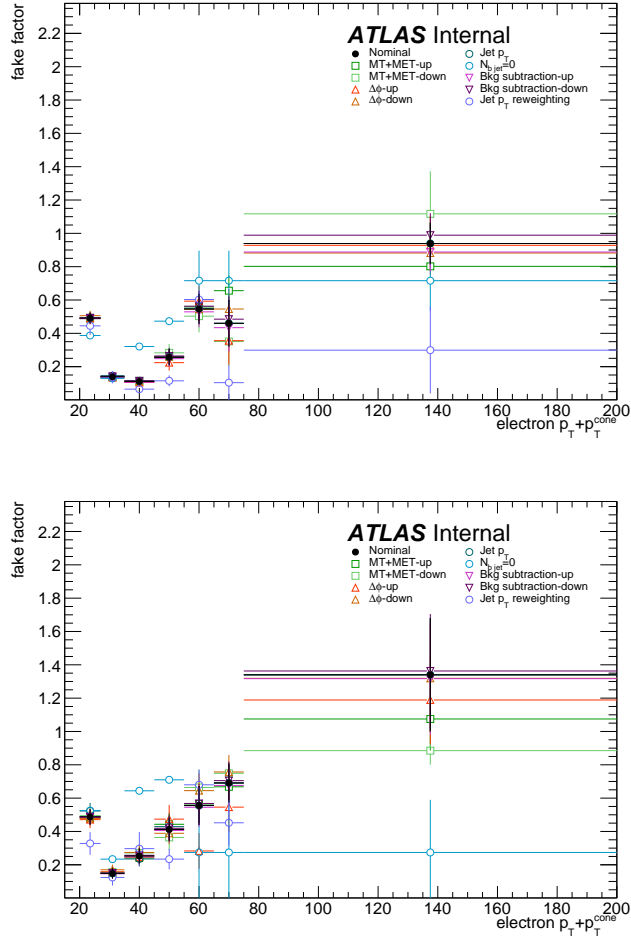


Figure 5.19: Systematic variations in the fake factor as a function of electron $p_T + p_T^{\text{cone}}$ in the central ($|\eta| < 1.37$, top) and forward ($|\eta| > 1.37$, bottom) regions of the detector. The individual fake factors obtained for each systematic variation are displayed with their statistical uncertainties.

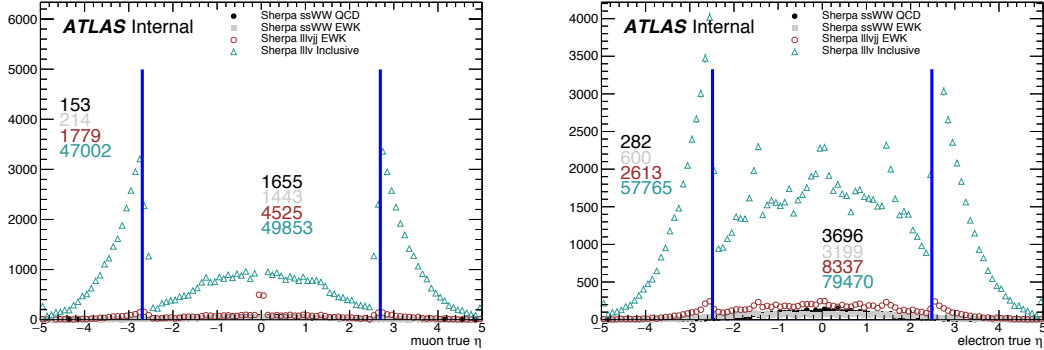


Figure 5.20: Pseudorapidity (η) distributions of truth muons (top) and electrons (bottom) for Sherpa $W^\pm W^\pm jj$ and WZ MC samples. The blue vertical lines represent the allowed η range for each lepton flavor. The numbers correspond to the number of raw MC events that fall within and outside of the allowed η range for each MC sample.

798 electrons can be found in Figures 5.21 and 5.23, respectively, and the distributions for $\Delta R(\mu, j)$ for
 799 muons can be found in Figure 5.22. Since all electrons have an associated jet in the calorimeters,
 800 the $\Delta R(e, j)$ variable is not a good quantity to use for this custom OR.

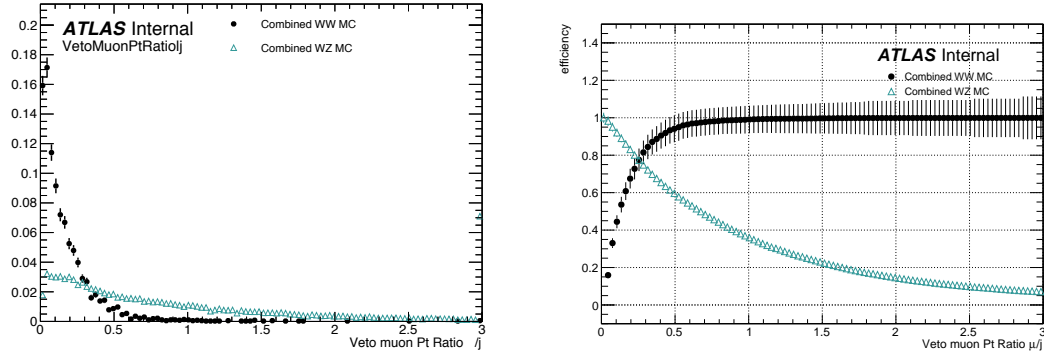


Figure 5.21: Distributions of $p_{T,\text{ratio}}(\mu, j)$ for EWK and QCD $W^\pm W^\pm jj$ signal (black) and WZ background (teal) for truth-matched third muons in events that pass the trilepton veto. Both distributions are normalized to unit area. The associated efficiency curves are on the right where efficiency is defined as the percentage of total events that would pass a cut on $p_{T,\text{ratio}}(\mu, j)$ at a given value on the x -axis.

801 A workingpoint for the Custom OR was chosen by requiring 90% signal retention for muons
 802 and 90% background rejection for electrons. The cut on electrons was allowed to be much tighter
 803 because the number of signal events with a third electron is considerably smaller than for muons.

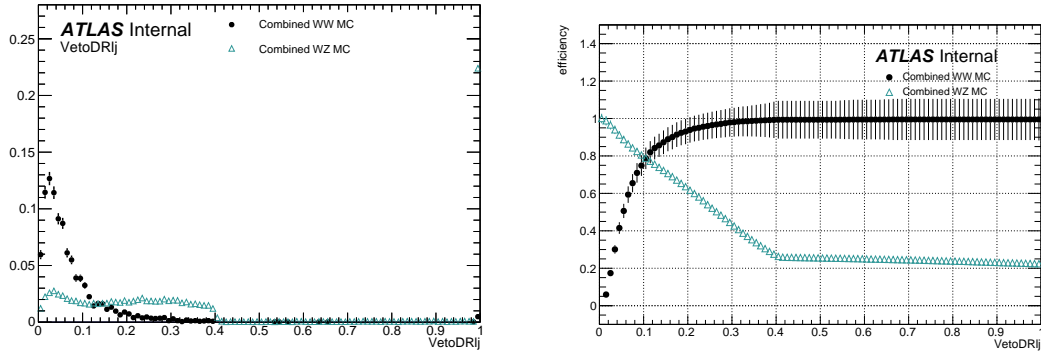


Figure 5.22: Distributions of $\Delta R(\mu, j)$ for EWK and QCD $W^\pm W^\pm jj$ signal (black) and WZ background (teal) for truth-matched third muons in events that pass the trilepton veto. Both distributions are normalized to unit area. The associated efficiency curves are on the right where efficiency is defined as the percentage of total events that would pass a cut on $\Delta R(\mu, j)$ at a given value on the x -axis.

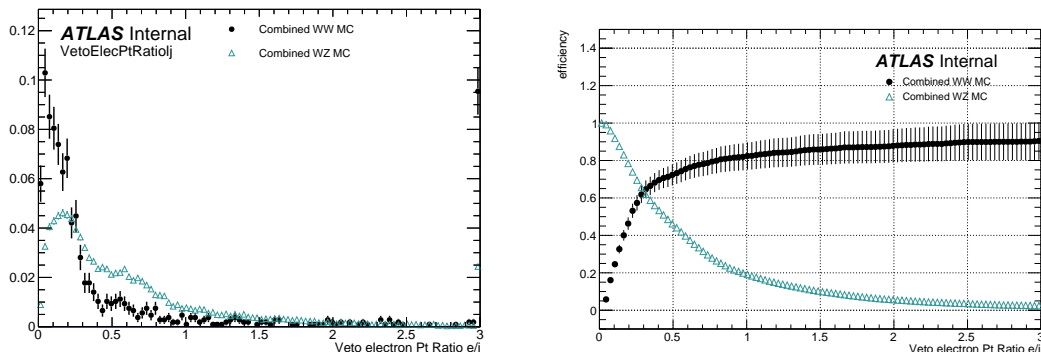


Figure 5.23: Distributions of $p_{T,\text{ratio}}(e, j)$ for EWK and QCD $W^\pm W^\pm jj$ signal (black) and WZ background (teal) for truth-matched third electrons in events that pass the trilepton veto. Both distributions are normalized to unit area. The associated efficiency curves are on the right where efficiency is defined as the percentage of total events that would pass a cut on $p_{T,\text{ratio}}(e, j)$ at a given value on the x -axis.

804 It should be re-emphasized the signal events that are present in Figures 5.21-5.23 do not represent
 805 the full set of signal events, but only those with a real third lepton (which must come from some
 806 source other than the signal $W^\pm W^\pm jj$ process). For muons, an or of $p_{T,\text{ratio}}(\mu, j)$ and $\Delta R(\mu, j)$ is
 807 used to maximize the third lepton acceptance due to correlations between the quantities, as shown
 808 in Figure 5.24; for electrons, only a cut on $p_{T,\text{ratio}}(e, j)$ is used. The Custom OR workingpoint is
 809 outlined in Table 5.13.

Custom OR Definition	
Muons	$p_{T,\text{ratio}}(\mu, j) > 0.40$ or $\Delta R(\mu, j) > 0.15$
Electrons	$p_{T,\text{ratio}}(e, j) > 0.18$

Table 5.13: Custom OR definition. Leptons must pass this selection in order to be counted for the trilepton veto.

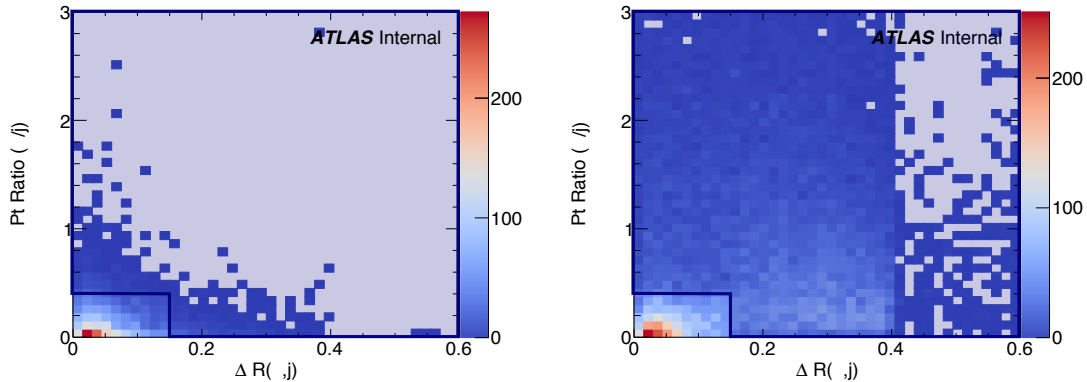


Figure 5.24: Two-dimensional plots of $p_{T,\text{ratio}}(\mu, j)$ vs $\Delta R(\mu, j)$ for truth-matched third muons in events that pass the trilepton veto for EWK and QCD $W^\pm W^\pm jj$ signal (left) and WZ background (right). The blue overlay indicates the area in which the third leptons will pass the custom OR and result in the event failing the trilepton veto.

810 Tests of the performance of the Custom OR yield promising results, with approximately 20%
 811 reduction in WZ background compared to less than 2% signal loss in the signal region. Unfortu-
 812 nately, due to differences between the primary analysis framework and the one used for testing,
 813 in practice the gains in WZ rejection are not nearly as substantial, and ultimately the Custom
 814 OR is not included in the final analysis. However, it is still a potentially useful tool for improving
 815 background rejection via lepton number vetoes in analyses with overly aggressive OR procedures.

816 **5.4 Cross section measurement**

817 Hello world!

818 **5.5 Results**

819 Results

820

CHAPTER 6

821

Prospects for same-sign WW at the High Luminosity LHC

822

823 On December 3, 2018, Run 2 of the LHC officially ended, and the collider was shut down to begin
 824 the first of two scheduled extended maintenance periods [45]. During these two long shutdowns,
 825 the Phase-I and Phase-II upgrades of the LHC and ATLAS will occur in order to prepare for the
 826 High-Luminosity LHC (HL-LHC) which is scheduled to begin operation in 2026 [46].

827 The HL-LHC is planned to run at a center-of-mass energy of $\sqrt{s} = 14$ TeV with an instantaneous
 828 luminosity of $\mathcal{L} = 5 \times 10^{34}$ cm $^{-2}$ s $^{-1}$ with up to 200 collisions per beam-crossing. Over the course
 829 of operation, the HL-LHC is expected to collect a total integrated luminosity of $\mathcal{L} = 3000$ fb $^{-1}$ by
 830 2035 [47]. **TODO: Compare to current LHC numbers?**

831 These run conditions will be much harsher than what ATLAS has experienced so far, and there
 832 are several upgrades planned for the detector to operate in the high luminosity environment. Most
 833 notably, the entire ID will be replaced with an all-silicon tracker which will extend the coverage from
 834 $|\eta| \leq 2.7$ up to $|\eta| \leq 4.0$. This will allow for reconstruction of charged particle tracks which can
 835 in turn be matched to clusters in the calorimeters for electron identification or forward jet tagging
 836 [48].

837 The upgraded detector, the higher beam energy, and the increased volume of data to be collected
 838 provides the opportunity to measure rarer processes with a much higher precision than what was
 839 possible in Run 1. Same-sign $W^\pm W^\pm jj$ production, is one such process. With greater statistics,
 840 the accuracy of the cross section measurement can be improved over the 13 TeV analysis detailed in
 841 Chapter 5, and it also will allow for more detailed physics studies, such as measuring the polarization
 842 of the W bosons. A measurement of the longitudinal polarization of the scattered W bosons has

843 not yet been possible, but it remains of great interest due to its sensitivity to electroweak symmetry
 844 breaking [49]. The analysis detailed in this chapter is based off of the 2018 ATLAS HL-LHC
 845 $W^\pm W^\pm jj$ prospects study [50] which is itself an extension of the 2017 ATLAS study [51]. **TODO:**
 846 mention CMS's study + yellow report?

847 6.0.1 Analysis Overview

848 The experimental signature of interest is identical to the 13 TeV analysis: two prompt leptons (either
 849 electrons or muons) with the same charge, missing transverse energy, and two high energy, forward
 850 jets. These jets are again required to have a large angular separation and a high combined invariant
 851 mass to preferentially select EWK- over QCD-produced $W^\pm W^\pm jj$ events.

852 Background processes are again similar to the 13 TeV analysis and are summarized again here.
 853 The dominant source of prompt background from $WZ+jets$ events where both bosons decay lepton-
 854ically. If the lepton from the Z -decay with opposite charge from the W falls outside of the detector
 855 acceptance or is not identified, the remainder could appear to be a $W^\pm W^\pm jj$ signal event. To a
 856 lesser extent, $ZZ+jets$ events can enter the signal region in much the same way provided two lep-
 857 tons are “lost”. Other prompt sources include $t\bar{t}+V$ and multiple parton interactions, however
 858 these processes do not contribute much. These prompt backgrounds are expected to contribute
 859 less than in Run 2 with the addition of forward tracking in the upgraded ATLAS detector. Jets
 860 mis-reconstructed as leptons or leptons from hadronic decays (such as $t\bar{t}$ and $W+jets$ production)
 861 comprise the non-prompt lepton background. Lastly, events with two prompt, opposite-charge elec-
 862 trons can appear as a same-sign event provided one of the electrons is mis-reconstructed as the
 863 wrong charge.

864 In this analysis, the EWK production of $W^\pm W^\pm jj$ is studied in the context of the planned
 865 HL-LHC run conditions and upgraded ATLAS detector. An optimized event selection (referred to
 866 as the *optimized selection*) is also explored in an effort to gain increased signal significance over
 867 the *default selection*. The cross section of the inclusive EWK production is measured for both the
 868 default and optimized selections, and the extraction of the longitudinal scattering significance is
 869 measured with the optimized selection.

870 6.1 Theoretical motivation

871 The theoretical motivation for studying the ssWW process—and VBS in general—is detailed in Sec-
 872 tion 5.0.1. Since it is specifically the scattering of *longitudinally polarized* vector bosons that violates

873 unitarity without a SM Higgs boson, a direct measurement of this cross section will be very useful
 874 for understanding how the Higgs unitarizes the process [49].

875 6.1.1 Experimental sensitivity to longitudinal polarization

876 **TODO:** mention that since there are so many polarization possibilities, a large integrated luminosity
 877 is needed to measure just one of them individually There are three possible polarization states for
 878 a massive vector boson: two transverse (+ or -) and one longitudinal (0). Therefore, in a system
 879 with two W bosons, the overall polarization can be purely longitudinal (00), purely transverse (++,
 880 --, and +-), or mixed (+0 and -0). The three combinations will be referred to as LL , TT , and
 881 LT respectively.

882 In order extract the longitudinal scattering component, it is necessary to find variables that
 883 distinguish the LL from the TT and LT . Several were studied, and those with the best discriminating
 884 power between the polarizations are the leading and subleading lepton p_T as well as the azimuthal
 885 separation ($|\Delta\phi_{jj}|$) of the two VBS jets. The LL events prefer lower p_T for both signal leptons
 886 (see Figure 6.1), which motivates keeping cuts on these quantities as low as possible in the event
 887 selection. In the case of $|\Delta\phi_{jj}|$, the LL events generally had a larger dijet separation (see Figure 6.2),
 888 and this variable is used in a binned likelihood fit to extract the longitudinal scattering significance.

889 6.2 Monte Carlo samples

890 As no real HL-LHC data will be available for many years, all signal and background processes
 891 are modeled using MC simulations generated at $\sqrt{s} = 14$ TeV, with the event yields scaled to the
 892 anticipated HL-LHC integrated luminosity of $\mathcal{L} = 3000 \text{ fb}^{-1}$. The MC samples used in the analysis
 893 are generated at particle-level and have not been run through the typical full simulation of the
 894 ATLAS detector. Instead, smearing functions derived from a **GEANT4** simulation of the upgraded
 895 ATLAS detector are used to estimate detector effects such as momentum resolution. In addition,
 896 pileup events are fully simulated. The MC samples used in this analysis are summarized in Table 6.1.

897 The signal sample consists of both VBS and non-VBS electroweak (EWK) $W^\pm W^\pm jj$ production,
 898 and it is simulated with the **Madgraph5_aMC@NLO** generator using the NNPDF3.0 PDF set and in-
 899 terfaced with **PYTHIA v8** [52] for hadronization and parton showering. To study the longitudinal
 900 polarization more directly, two additional **Madgraph5_aMC@NLO** $W^\pm W^\pm jj$ samples are used: one
 901 containing only the longitudinal contribution (LL) and a second containing the transverse (TT) and
 902 mixed (LT) contributions.

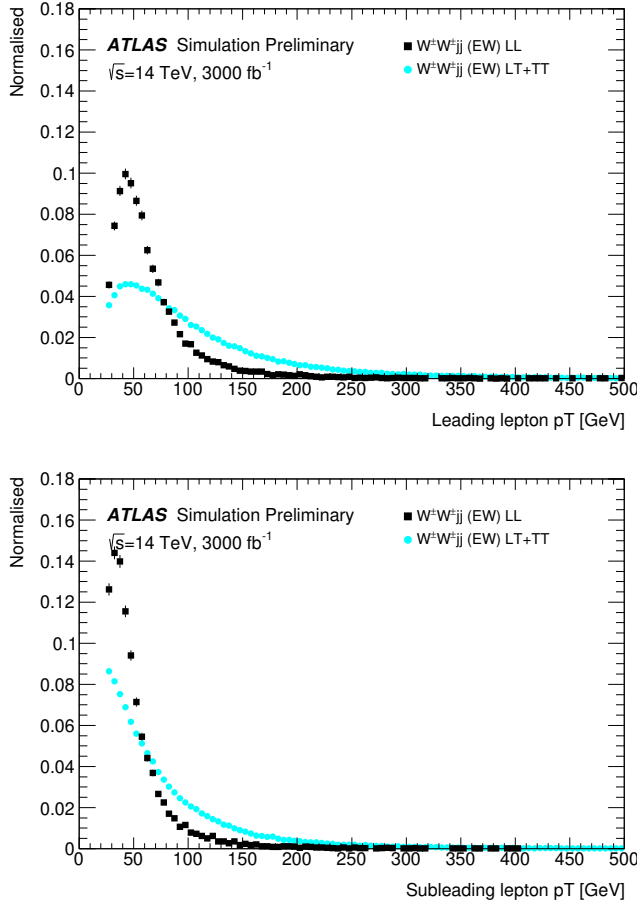


Figure 6.1: Comparison of the leading (top) and subleading (bottom) lepton p_T distributions for purely longitudinal (LL, black) and mixed polarization (LT+TT, cyan) $W^\pm W^\pm jj$ events.

903 There are many other processes that can produce the same final state as the $W^\pm W^\pm jj$ and
 904 must also be accounted for using MC simulations. WZ events are generated using **SHERPA v2.2.0**,
 905 which includes up to one parton at NLO in the strong coupling constant and up to three addi-
 906 tional partons at LO. Both EWK and QCD production are included in these samples. ZZ and
 907 triboson VVV ($V = W, Z$) events are generated using **SHERPA v2.2.2** with up to two additional
 908 partons in the final state. For the triboson backgrounds, the bosons can decay leptonically or
 909 hadronically. $W+jets$ backgrounds are generated for electron, muon, and tau final states at LO
 910 with **Madgraph5_aMC@NLO** and the **NNPDF3.0** set with showering from **PYTHIA v8**. $Z+jets$ events are
 911 produced using **POWHEG-BOX v2** and the **CT10** PDF set interfaced with **PYTHIA v8**. Finally, $t\bar{t}$ and

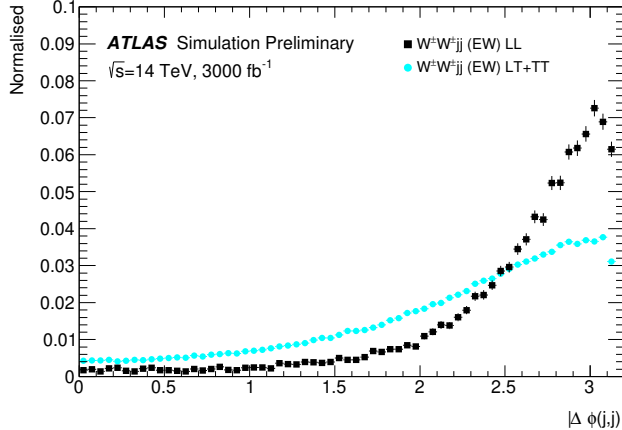


Figure 6.2: Comparison of the azimuthal dijet separation ($|\Delta\phi_{jj}|$) for purely longitudinal (LL, black) and mixed polarization (LT+TT, cyan) $W^\pm W^\pm jj$ events.

Process	Generator	Comments
$W^\pm W^\pm jj$ (EWK)	Madgraph5_aMC@NLO	Signal sample
$W^\pm W^\pm jj$ (QCD)	Madgraph5_aMC@NLO	
$W^\pm W^\pm jj$ (LL)	Madgraph5_aMC@NLO	Pure longitudinal polarization sample
$W^\pm W^\pm jj$ (TT+LT)	Madgraph5_aMC@NLO	Mixed and transverse polarization sample
Diboson	SHERPA v2.2.0	WZ events
	SHERPA v2.2.2	ZZ events
Triboson	SHERPA v2.2.2	
$W+jets$	Madgraph5_aMC@NLO	
$Z+jets$	POWHEG-BOX v2	
$t\bar{t}$	POWHEG-BOX	
Single top	POWHEG-BOS	

Table 6.1: Summary of MC samples used in the analysis.

single-top events are generated using POWHEG-BOX with showering from PYTHIA v6.

6.3 Background estimations

In this analysis, all background contributions are estimated using MC simulations. Backgrounds such as electron charge misidentification and fake electrons from jets (which are traditionally estimated using data-driven techniques) are estimated using a set of parameterization functions applied to the MC. These functions calculate the probability that an electron is assigned the wrong charge or a jet is mis-reconstructed as an electron parameterized by the p_T and η of the electron or jet. The probabilities are derived from studies on expected electron performance with the upgraded ATLAS

920 detector [53].

921 Processes involving two W and Z bosons are grouped together as *diboson* backgrounds, with the
 922 exception of $W^\pm W^\pm jj$ events produced via QCD interactions, which are kept separate. Similarly,
 923 all backgrounds with three vector bosons are combined and labeled as *triboson*. Any $W+jets$ or top
 924 events that pass selection and do not contain a fake electron, as well as any $Z+jets$ events without an
 925 electron identified as having its charge misidentified are combined as *other non-prompt* backgrounds.

926 6.3.1 Truth-based isolation

927 To properly calculate particle isolation, it requires information from several detector subsystems
 928 including tracking and calorimeter responses. Since the MC samples used in this analysis have not
 929 been run through a full detector simulation, it is not possible to construct the canonical isolation
 930 variables used in analyses. At truth-level, this is generally not a serious concern as p_T signal leptons
 931 tend to be well isolated to begin with. However, isolation is one of the most powerful tools for
 932 rejecting leptons from non-prompt sources such as top events, which are produced in association
 933 with additional nearby particles from b and c quark decays. In this analysis, with the absence of
 934 any sort of isolation requirement, contributions from top backgrounds (including single top, $t\bar{t}$ and
 935 $t\bar{t} + V$) are more than an order of magnitude higher than expected.

936 As a result, it is necessary to find one or more quantities that are comparable to the isolation
 937 information that is available in fully-simulated samples. Analogues to track- and calorimeter-based
 938 isolation variables are constructed by summing the momentum and energy, respectively, of stable
 939 truth particles with $p_T > 1$ GeV within a specified radius of each signal lepton. For the track-
 940 based isolation, only charged truth particles are used; both charged and neutral particles (excluding
 941 neutrinos) are included for the calorimeter-based isolation. Ultimately, a set of isolation cuts are
 942 chosen that are similar to those recommended by ATLAS for Run 2 analyses. The truth-based
 943 isolation requirements are listed in Table 6.2.

	Electron Isolation	Muon Isolation
Track-based isolation cone size	$\Delta R < 0.2$	$\Delta R < 0.3$
Track-based isolation requirement	$\sum p_T/p_T^e < 0.06$	$\sum p_T/p_T^\mu < 0.04$
Calorimeter-based isolation cone size	$\Delta R < 0.2$	$\Delta R < 0.2$
Calorimeter-based isolation requirement	$\sum E_T/p_T^e < 0.06$	$\sum E_T/p_T^\mu < 0.15$

Table 6.2: Truth-based isolation requirements for electrons and muons.

944 The truth-based isolation requirement reduces the top background by over 99%, and the per-

945 centage of the total background consisting of top events is reduced from 83% to 2%. Additional
 946 details on the truth-based isolation studies are presented in Appendix A.

947 6.4 Object and event selection

948 6.4.1 Object selection

949 Electrons and muons are preselected to have $p_T > 7$ and 6 GeV, respectively, and $|\eta| \leq 4.0$. The
 950 likelihood of a given lepton to pass the trigger and identification requirements is estimated by
 951 calculating an efficiency dependent on the p_T and η of the lepton. The leptons are also required to
 952 pass the isolation criteria detailed in Table 6.2. Jets that have been tagged as a fake electron by the
 953 functions described in Section 6.3 are treated as electrons for the purpose of the object selection and
 954 are subject to the same criteria. In order to be considered a signal lepton, an additional requirement
 955 of $p_T > 25$ GeV is applied on top of the preselection. The two highest p_T leptons passing this
 956 selection are chosen to be the leading and subleading signal leptons.

957 Jets are clustered using the anti- k_t algorithm [37] from final-state particles within a radius of
 958 $\Delta R = 0.4$ (excluding muons and neutrinos). Jets are required to have $p_T > 30$ GeV and lie within
 959 $|\eta| < 4.5$, with an additional cut of $p_T > 70$ GeV for jets above $|\eta| \geq 3.8$ in order to suppress jets
 960 from pileup interactions. Jets overlapping with a preselected electron within $\Delta R(e, j) < 0.05$ are
 961 removed in order to prevent double counting. The two highest p_T jets are defined as the leading
 962 and subleading *tag jets*.

963 6.4.2 Event selection

964 The default event selection is summarized in Table 6.3 and described here. Exactly two signal
 965 leptons are required with the same electric charge and separated from each other by $\Delta R(ll) > 0.3$.
 966 In order to suppress contributions from Drell-Yan backgrounds, the two signal leptons must have
 967 an invariant mass m_{ll} greater than 20 GeV. Additionally, if both signal leptons are electrons, their
 968 mass must be at least 10 GeV from the Z -boson mass in order to reduce background from Z -boson
 969 decays⁹. The event is required to have at least 40 GeV of missing transverse energy (E_T^{miss}) to
 970 account for the two neutrinos from the W decays. Events with additional preselected leptons are
 971 vetoed, which greatly reduces WZ and ZZ backgrounds.

⁹The electron charge misidentification rate in the upgraded ATLAS detector is estimated to be high enough that contributions from $Z \rightarrow ee$ backgrounds are non-negligible.

972 Each event must have at least two jets, and both tag jets are required to not overlap with the
 973 signal leptons, and there is a veto on events with one or more b -jets. In order to preferentially select
 974 EWK production, the tag jets are also required to have a large separation between them and a large
 975 invariant mass. Finally, a cut on the lepton centrality¹⁰, ζ , defined in Equation 6.1 enhances the
 976 EWK $W^\pm W^\pm jj$ signal.

$$\zeta = \min[\min(\eta_{\ell 1}, \eta_{\ell 2}) - \min(\eta_{j 1}, \eta_{j 2}), \max(\eta_{j 1}, \eta_{j 2}) - \max(\eta_{\ell 1}, \eta_{\ell 2})] \quad (6.1)$$

Selection requirement	Selection value
Lepton kinematics	$p_T > 25 \text{ GeV}$ $ \eta \leq 4.0$
Jet kinematics	$p_T > 30 \text{ GeV}$ for $ \eta \leq 4.5$ $p_T > 70 \text{ GeV}$ for $ \eta > 3.8$
Dilepton charge	Exactly two signal leptons with same charge
Dilepton separation	$\Delta R_{l,l} \geq 0.3$
Dilepton mass	$m_{ll} > 20 \text{ GeV}$
Z boson veto	$ m_{ee} - m_Z > 10 \text{ GeV}$ (ee -channel only)
E_T^{miss}	$E_T^{\text{miss}} > 40 \text{ GeV}$
Jet selection	At least two jets with $\Delta R_{l,j} > 0.3$
b jet veto	$N_{b\text{-jet}} = 0$
Dijet separation	$\Delta\eta_{jj} > 2.5$
Trilepton veto	No additional preselected leptons
Dijet mass	$m_{jj} > 500 \text{ GeV}$
Lepton-jet centrality	$\zeta > 0$

Table 6.3: Summary of the signal event selection.

977 6.5 Selection optimization

978 An upgraded detector along with an increase in center of mass energy and integrated luminosity
 979 provides an opportunity to study whether the event selection can be optimized to improve the signal
 980 to background ratio.

981 6.5.1 Random grid search algorithm

982 The chosen method for optimizing the event selection is a cut-based algorithm known as the Random
 983 Grid Search (RGS) [54]. Consider a simple case of two variables x and y chosen to differentiate signal

¹⁰ ζ is a measurement of whether the two signal leptons lie between the two tagging jets in η , as is preferred by the VBS topology.

984 from background. In order to be considered a signal event, a given event would be required to pass
 985 a set of selection criteria, called a *cut point*: $c = \{x > x_c, y > y_c\}$. A simple method to choose the
 986 optimal cut point (i.e. the “best” values of the cuts x_c and y_c) would be to construct an $n \times m$
 987 rectangular grid in x and y consisting of points $(x_0, y_0), (x_1, y_1), \dots, (x_n, y_m)$, as in Figure 6.3. One
 988 can then choose a cut point $c_k = \{x > x_i, y > y_j\}$ that maximizes the signal significance as measured
 989 by a chosen metric. This would be considered a *rectangular grid search*.

990 While effective in principle, a rectangular grid search comes with two major drawbacks:

- 991 1. The algorithm scales exponentially as the number of variables to be optimized increases, as
 992 this is effectively increasing the dimensionality of the grid. In the simple case of a square grid
 993 with N bins per variable v , the number of cut points to be evaluated grows as N^v .
- 994 2. Signal and background samples are rarely evenly distributed over the entire grid, resulting
 995 in many cut points being sub-optimal and evaluating them would be a waste of computing
 996 resources.

997 To combat these limitations, the RGS algorithm constructs a grid of cut points directly from
 998 the signal sample itself. In the two-dimensional example, this means that the variables x_i and y_j
 999 making up the cut point $c_k = \{x > x_i, y > y_j\}$ take their values directly from a given signal event.
 1000 This has the benefit of creating a *random grid* of cut points that is biased towards regions of high
 1001 signal concentration by construction. This reduces the need for exponentially increasing numbers of
 1002 cut points while ensuring that computing resources are not wasted in regions with few to no signal
 1003 events. An example of the the two-dimensional random grid is shown in Figure 6.4.

1004 Once the random grid of cut points is constructed, the optimal cut point can be chosen using any
 1005 number of metrics, such as signal to background ratio. For the purpose of the $W^\pm W^\pm jj$ upgrade
 1006 study, the optimal cut point is chosen to be the one that mazimizes the signal significance Z as
 1007 defined in Equation 6.2 [55].

$$Z = \sqrt{2 \left[(s + b) \ln \left(\frac{s + b}{b_0} \right) + b_0 - s - b \right] + \frac{(b - b_0)^2}{\sigma_b^2}} \quad (6.2)$$

1008 where s and b are the number of signal and background events, respectively, σ_b is the total uncertainty
 1009 on the background, and b_0 is defined as:

$$b_0 = \frac{1}{2} \left(b - \sigma_b^2 + \sqrt{(b - \sigma_b^2)^2 + 4(s + b)\sigma_b^2} \right) \quad (6.3)$$

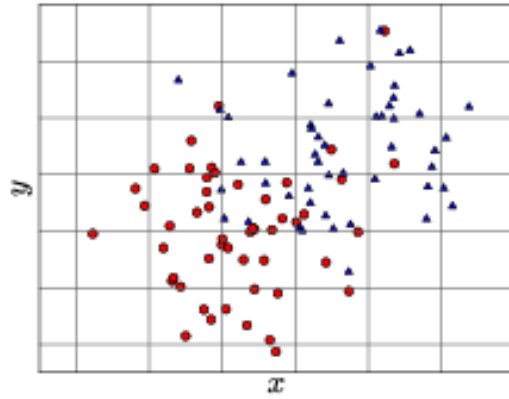


Figure 6.3: A visual representation of a rectangular grid search algorithm. The signal events are the blue triangles, and the red circles are the background events. **TODO: replace with own figure**

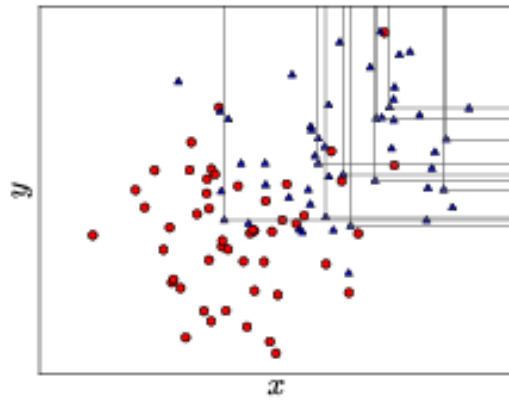


Figure 6.4: A visual representation of a random grid search algorithm. The signal events are the blue triangles, and the red circles are the background events. **TODO: replace with own figure**

1010 In the case where the background is known precisely (i.e. $\sigma_b = 0$), Equation 6.2 simplifies to

$$Z = \sqrt{2 \left(b[(1 + s/b) \ln(1 + s/b) - s/b] \right)} \quad (6.4)$$

1011 which further reduces to the familiar $Z = s/\sqrt{b}$ for the case when $s \ll b$.

1012 6.5.2 Inputs to the optimization

1013 In order to train the RGS, signal and background samples are prepared from events passing the
 1014 event selection outlined in Table 6.3 up through the b -jet veto. The signal sample is chosen to be
 1015 the longitudinally polarized $W^\pm W^\pm jj$ EWK events, and the transverse and mixed polarizations
 1016 are treated as background along with $W^\pm W^\pm jj$ events from QCD interactions and the traditional
 1017 backgrounds listed in Section 6.3. Splitting the inclusive $W^\pm W^\pm jj$ EWK events by polarization
 1018 allows the optimization to favor the longitudinally polarized events as much as possible, even though
 1019 they both contribute to the EWK signal.

1020 The following variables are chosen for optimization:

- 1021 • Leading lepton p_T
- 1022 • Dilepton invariant mass (m_{ll})
- 1023 • Leading and subleading jet p_T
- 1024 • Dijet invariant mass (m_{jj})
- 1025 • Lepton-jet centrality (ζ)

1026 Subleading lepton p_T is omitted as it is desirable to keep the cut value as low as possible due to
 1027 its sensitivity to the longitudinal polarization (as discussed in Section 6.1.1). Additionally, the dijet
 1028 separation $\Delta\eta_{jj}$ was included in the optimization originally, however it was dropped from the list due
 1029 to the cut value being motivated by differences between EWK and QCD produced $W^\pm W^\pm jj$ events.

1030 Two additional constraints were imposed when selecting the optimal cut point:

- 1031 1. At least 1000 signal events must survive in order to prevent the optimization from being too
 1032 aggressive and unnecessarily reducing signal statistics.
- 1033 2. The dijet invariant mass may only vary within a 50 GeV range of the default value (from
 1034 450 – 550 GeV) due to the cut being physically motivated by the VBS event topology (see
 1035 Section 5.0.2).

1036 Lastly, the signal significance is calculated without taking into account the uncertainty of the
 1037 background using Equation 6.4. This is due to the fact that the statistical uncertainties of the fake
 1038 electron and charge misidentification backgrounds are quite large, owing to poor MC statistics in a
 1039 few of the samples. If Equation 6.2 were used instead, the optimization will cut unreasonably hard
 1040 against these backgrounds. Since Monte Carlo statistics is not expected to be a limiting factor when
 1041 this analysis is performed at the HL-LHC, it is more realistic to simply ignore these large statistical
 1042 uncertainties for the purpose of the optimization.

1043 6.5.3 Results of the optimization

1044 Ultimately, the random grid is constructed from over 38,000 LL-polarized $W^\pm W^\pm jj$ events in the
 1045 six variables listed above. After applying the constraints, the optimal cut point reduces the total
 1046 background from 9900 to 2310 while reducing the signal from 3489 to 2958. This corresponds to
 1047 an increase in signal significance from $Z = 33.26$ to $Z = 52.63$ as calculated by Equation 6.4. The
 1048 updates to the event selection are listed in Table 6.4.

1049 The large reduction in the background is primarily a result of the increase in the leading and
 1050 subleading jet p_T from 30 GeV to 90 GeV and 45 GeV, respectively. As can be seen in Figure 6.7,
 1051 this increase removes a significant portion of the backgrounds from jets faking electrons and charge
 1052 mis-ID. Additionally, the loosening of the lepton-jet centrality cut ζ allows more signal events to
 1053 survive the event selection (see Figure 6.9). Other changes to the event selection are minor and do
 1054 not individually have a large impact on the signal or background yields.

1055 The full event yields after optimization as well as the cross section measurement are detailed
 1056 alongside those using the default selection in Section 6.6.

1057 TODO: It's a bit awkward to reference the results of the default/optimized before they're prop-
 1058 erly presented. Maybe move the sections around? not sure...

Selection requirement	Selection value
Lepton kinematics	$p_T > 28$ GeV (leading lepton only)
Jet kinematics	$p_T > 90$ GeV (leading jet) $p_T > 45$ GeV (subleading jet)
Dilepton mass	$m_{ll} > 28$ GeV
Dijet mass	$m_{jj} > 520$ GeV
Lepton-jet centrality	$\zeta > -0.5$

Table 6.4: Updates to the $W^\pm W^\pm jj$ event selection criteria after optimization. Cuts not listed remain unchanged from the default selection in Table 6.3.

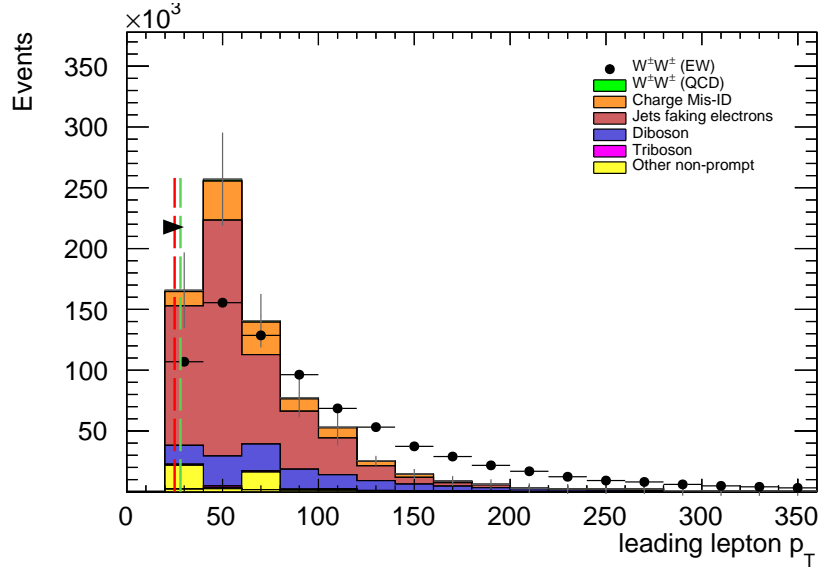


Figure 6.5: Leading lepton p_T distribution. The default and optimized cuts are represented by the red and green dashed lines, respectively. The $W^\pm W^\pm jj$ EWK signal (black points) is normalized to the same area as the sum of the backgrounds (colored histogram). **TODO:** Move to appendix or omit

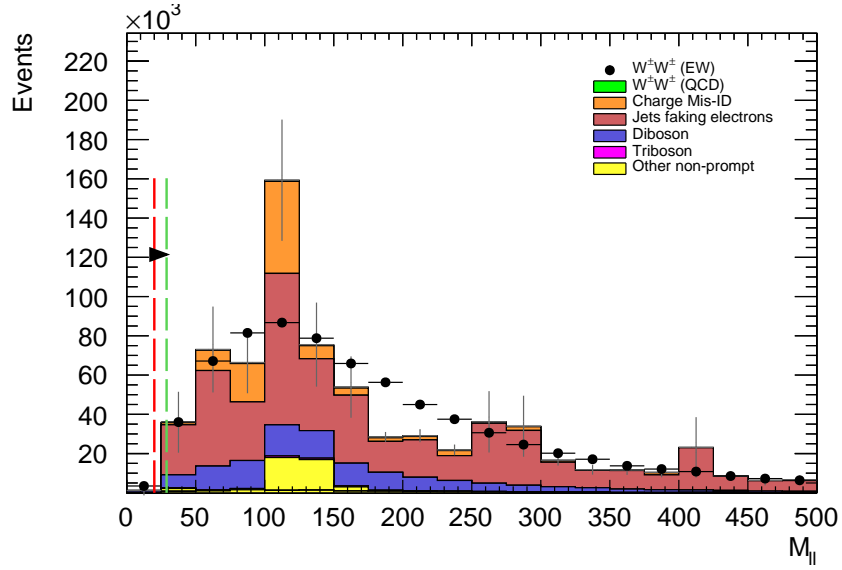


Figure 6.6: Dilepton invariant mass distribution. The default and optimized cuts are represented by the red and green dashed lines, respectively. The $W^\pm W^\pm jj$ EWK signal (black points) is normalized to the same area as the sum of the backgrounds (colored histogram). **TODO:** Move to appendix or omit

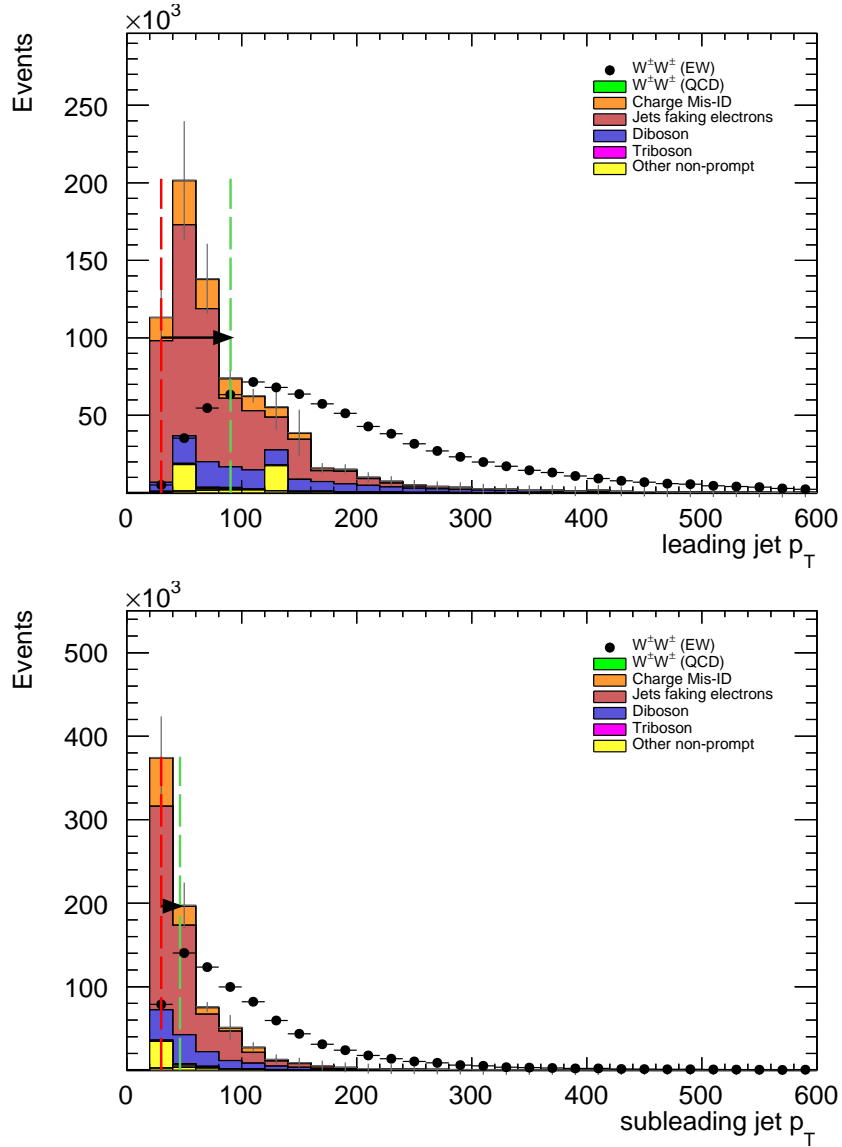


Figure 6.7: Leading (top) and subleading (bottom) jet p_T distributions. The default and optimized cuts are represented by the red and green dashed lines, respectively. The $W^\pm W^\pm jj$ EWK signal (black points) is normalized to the same area as the sum of the backgrounds (colored histogram).

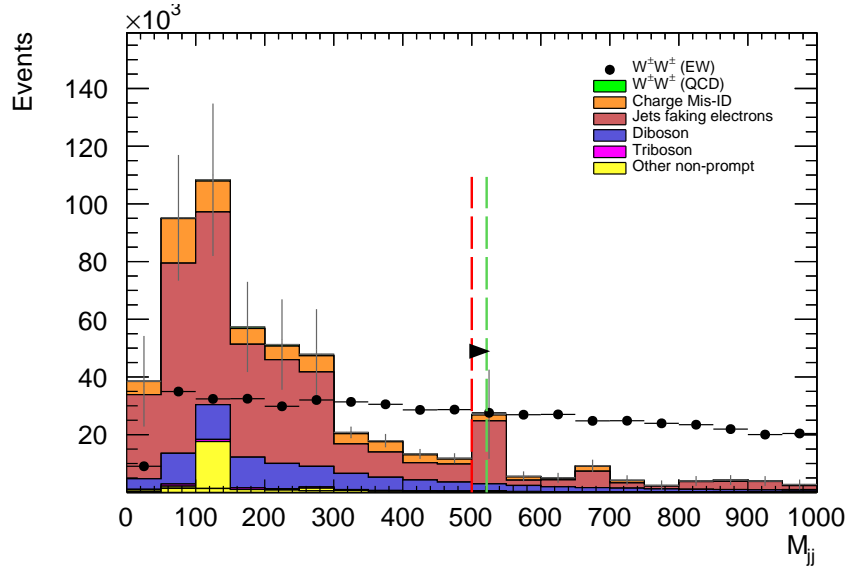


Figure 6.8: Dijet invariant mass distribution. The default and optimized cuts are represented by the red and green dashed lines, respectively. The $W^\pm W^\pm jj$ EWK signal (black points) is normalized to the same area as the sum of the backgrounds (colored histogram). **TODO:** Move to appendix or omit

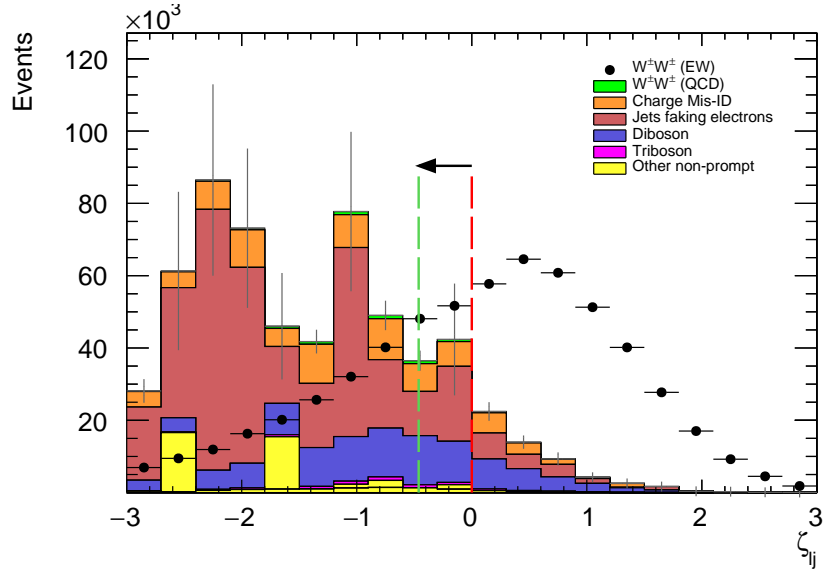


Figure 6.9: Lepton-jet centrality distribution. The default and optimized cuts are represented by the red and green dashed lines, respectively. The $W^\pm W^\pm jj$ EWK signal (black points) is normalized to the same area as the sum of the backgrounds (colored histogram).

1059 **6.6 Results**

1060 **6.6.1 Event yields**

1061 After applying the full event selection, the analysis is broken down into four channels based off of
 1062 the flavor of the signal leptons: $\mu\mu$, ee , μe , and $e\mu$. The full signal and background event yields are
 1063 shown in Table 6.5 for each channel separately and combined using the default event selection. 3489
 1064 EWK $W^\pm W^\pm jj$ events are expected compared to 9900 background events. The dominant sources
 1065 of background are jets faking electrons followed by charge misidentification and diboson processes.
 1066 Triboson events, QCD $W^\pm W^\pm jj$, and other non-prompt sources make up approximately 5% of the
 1067 total background combined.

	All channels	$\mu\mu$	ee	μe	$e\mu$
$W^\pm W^\pm jj$ (QCD)	206.4	91.1	22.8	38.4	54.1
Charge Misidentification	2300	0.0	2100	90	160
Jets faking electrons	5000	0.0	3400	1200	340
$WZ + ZZ$	2040	500	438	423	680
Tribosons	115	47	15.4	21.6	31.2
Other non-prompt	210	110	20	60	27
Total Background	9900	750	6000	1900	1290
Signal $W^\pm W^\pm jj$ (EWK)	3489	1435	432	679	944

Table 6.5: Signal and background event yields using the default event selection for an integrated luminosity of $\mathcal{L} = 3000 \text{ fb}^{-1}$. Events containing a fake or charge-flipped electron are removed from their respective sources and combined into a single entry each.

1068 The event yields for the optimized selection detailed in Section 6.5.3 are listed in Table 6.6. After
 1069 optimization, 2958 signal events and just 2310 background events are expected. Diboson events are
 1070 now the primary source of background, as the optimization greatly reduces the fake and charge
 1071 misidentification backgrounds. As discussed earlier, the increase in the leading and subleading jet
 1072 p_T cuts as well as the loosening of the centrality cut are most responsible for the changes in the
 1073 signal and background yields; distributions of these quantities using the default and the optimized
 1074 event selections can be found in Figures 6.10, 6.11, and 6.12, respectively.

1075 It is important to note, however, that the MC sample used to estimate $Z+\text{jets}$ events suffers from
 1076 poor statistics which results in large per-event weights once scaled to $\mathcal{L} = 3000 \text{ fb}^{-1}$. This sample
 1077 contributes heavily to the fake and charge misidentification backgrounds, and a handful of these
 1078 events being cut out by the optimization contributes has a large effect on the dramatic reduction
 1079 of these backgrounds. As a result, these particular optimized results are likely overly optimistic.
 1080 However, given proper MC statistics, it is still expected that the optimization will outperform the

	All channels	$\mu\mu$	ee	μe	$e\mu$
$W^\pm W^\pm jj$ (QCD)	168.7	74.6	19.7	32.2	42.2
Charge Misidentification	200	0.0	11	30	160
Jets faking electrons	460	0.0	130	260	70
$WZ + ZZ$	1286	322	289	271	404
Tribosons	76	30.1	9.6	15.1	21.6
Other non-prompt	120	29	16.6	50	19
Total Background	2310	455	480	660	710
Signal $W^\pm W^\pm jj$ (EWK)	2958	1228	380	589	761

Table 6.6: Signal and background event yields using the optimized event selection for an integrated luminosity of $\mathcal{L} = 3000 \text{ fb}^{-1}$. Events containing a fake or charge-flipped electron are removed from their respective sources and combined into a single entry each.

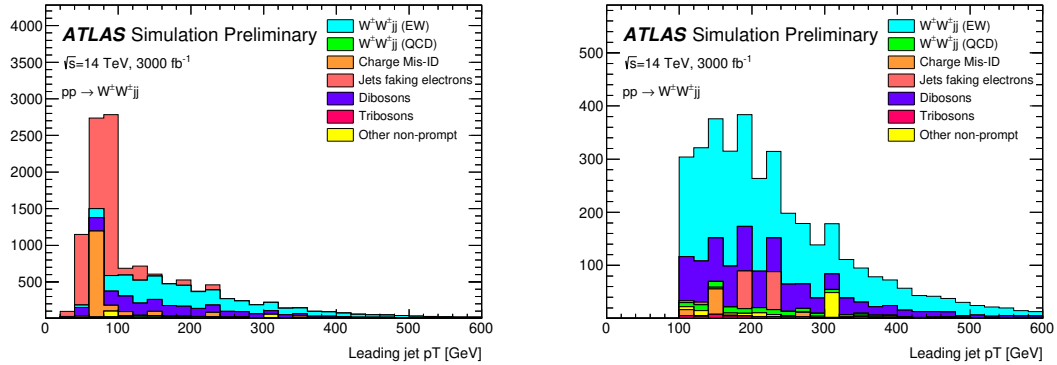


Figure 6.10: p_T distributions for the leading jet using the default (left) and optimized (right) event selections for all channels combined.

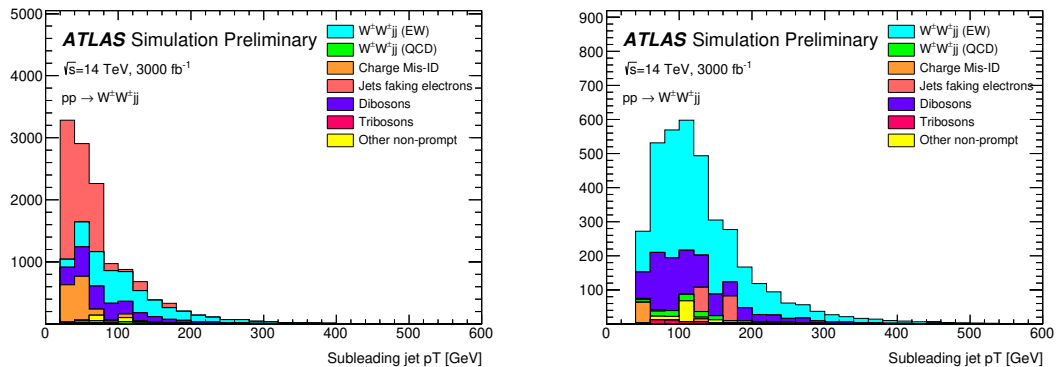


Figure 6.11: p_T distributions for the subleading jet using the default (left) and optimized (right) event selections for all channels combined.

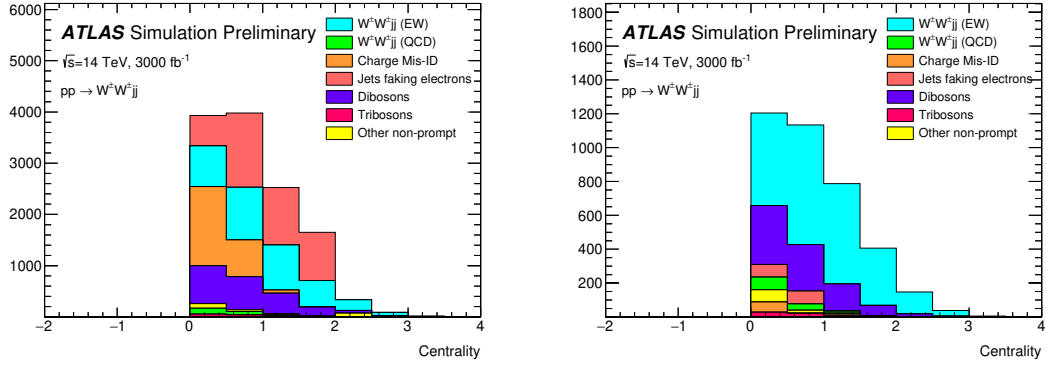


Figure 6.12: p_T distributions for lepton-jet centrality ζ using the default (left) and optimized (right) event selections for all channels combined.

1081 default selection.

1082 6.6.2 Uncertainties

1083 **TODO:** Ask for details on how some of these uncertainties were calculated – specifically the fakes and
 1084 charge mis-ID The uncertainties considered for the analysis are summarized in Table 6.7. Values for
 1085 experimental systematics on the trigger efficiency, lepton and jet reconstruction, and flavor tagging
 1086 are taken directly from the 13 TeV analysis [1]. The rate uncertainties for the background processes
 1087 are halved from the 13 TeV values.

Source	Uncertainty (%)
$W^\pm W^\pm jj$ (EWK)	3
Luminosity	1
Trigger efficiency	0.5
Lepton reconstruction and identification	1.8
Jets	2.3
Flavor tagging	1.8
Jets faking electrons	20
Charge misidentification	25
$W^\pm W^\pm jj$ (QCD)	20
Top	15
Diboson	10
Triboson	15

Table 6.7: Summary of estimated experimental and rate uncertainties.

1088 **6.6.3 Cross section measurement**

1089 The cross section is calculated using the same method as in the 13 TeV analysis, detailed in Chap-
 1090 ter 5. **TODO: update from chapter reference to subsection reference (once it's written)...** Once
 1091 again, each of the four lepton flavor channels is further split by charge (i.e. $\mu\mu \rightarrow \mu^+\mu^+ + \mu^-\mu^-$),
 1092 as this increases the sensitivity of the analysis. Each channel's m_{jj} distribution is combined in a
 1093 profile likelihood fit to extract the EWK $W^\pm W^\pm jj$ production cross section. The expected cross
 1094 section calculated using the default event selection is:

$$\sigma_{W^\pm W^\pm jj}^{\text{expected}} = 16.89 \pm 0.36 \text{ (stat)} \pm 0.53 \text{ (theory)} \pm 0.84 \text{ (syst)} \text{ fb} \quad (6.5)$$

1095 The expected cross section calculated using the optimized event selection is:

$$\sigma_{W^\pm W^\pm jj}^{\text{expected}} = 16.94 \pm 0.36 \text{ (stat)} \pm 0.53 \text{ (theory)} \pm 0.78 \text{ (syst)} \text{ fb} \quad (6.6)$$

1096 The optimized selection should not change the measured value of the cross section, and indeed both
 1097 are consistent with within uncertainties. The systematic uncertainty is reduced by approximately 7%
 1098 with the optimized selection. Projections of the total uncertainty on the cross section as a function
 1099 of integrated luminosity made by **TODO: how was this made?** is shown in Figure 6.13. As the
 1100 integrated luminosity increases past $\mathcal{L} > 3000 \text{ fb}^{-1}$, the statistical uncertainty reduces faster than
 1101 the systematic uncertainties. However, the total uncertainty is expected to reduce by less than a
 1102 percent with increased luminosity past the planned 3000 fb^{-1} .

1103 **6.6.4 Longitudinal scattering significance**

1104 **TODO: get some details on how this was all done...** The longitudinal scattering significance is
 1105 extracted from the $|\Delta\phi_{jj}|$ distribution using a simultaneous binned likelihood fit. In order to increase
 1106 sensitivity, the $|\Delta\phi_{jj}|$ distribution was split into two bins in m_{jj} , and an additional cut on the
 1107 pseudorapidity of the subleading lepton was applied ($|\eta| < 2.5$) to reduce background from fake and
 1108 charge misidentification. The $|\Delta\phi_{jj}|$ distributions used in the fit are shown in Figure 6.14. Due to
 1109 limited statistics, the four lepton flavor channels were not split by charge. The expected significance
 1110 of the $W_L^\pm W_L^\pm jj$ process is 1.8σ with a precision of 47% on the measurement. Projections of the
 1111 expected significance as a function of integrated luminosity is shown in Figure 6.15.

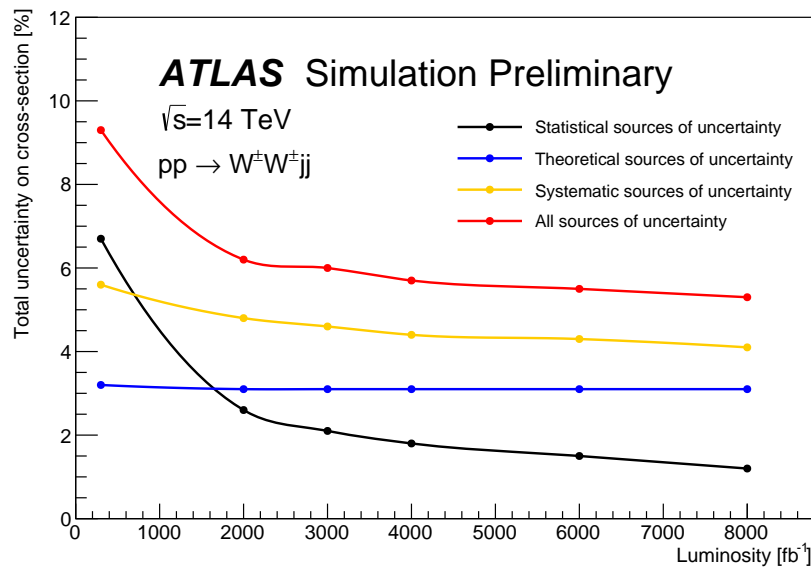


Figure 6.13: Projections of the statistical (black), theoretical (blue), systematic (yellow), and total (red) uncertainties on the measured cross section as a function of integrated luminosity using the optimized event selection.

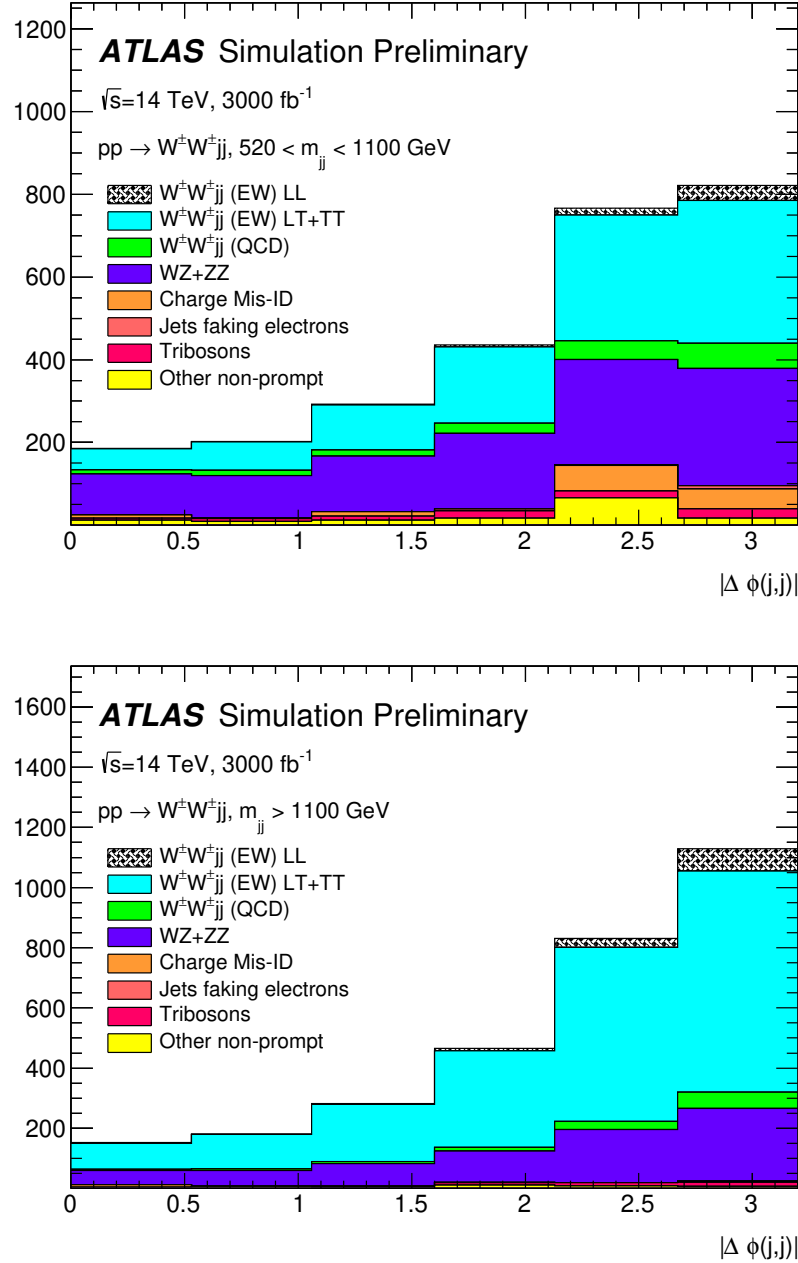


Figure 6.14: Dijet azimuthal separation ($|\Delta\phi_{jj}|$) for the low m_{jj} region ($520 < m_{jj} < 1100 \text{ GeV}$, top) and the high m_{jj} region ($m_{jj} > 1100 \text{ GeV}$, bottom). The purely longitudinal (LL, gray) is plotted separately from the mixed and transverse (LT+TT, cyan) polarizations.

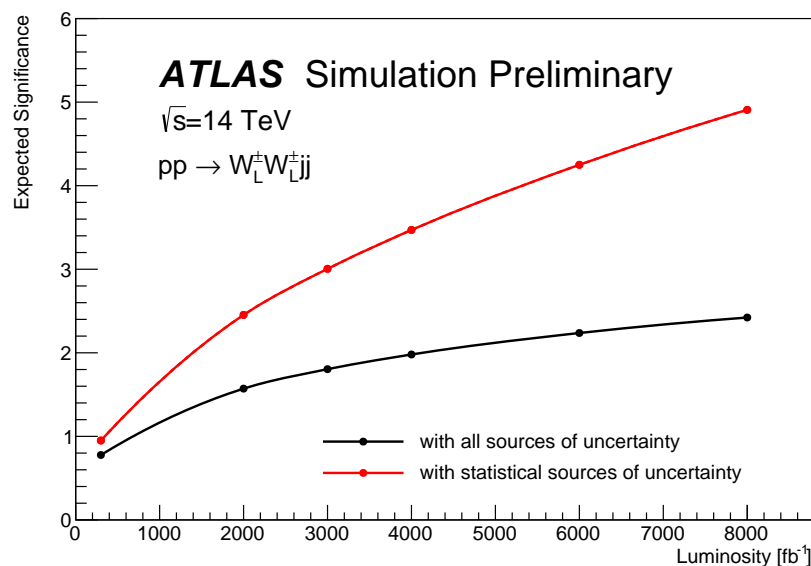


Figure 6.15: Projections of the expected longitudinal scattering significance as a function of integrated luminosity when considering all sources of uncertainties (black) or only statistical uncertainties (red).

1112

CHAPTER 7

1113

Conclusion

1114 Here's where you wrap it up.

1115 **Looking Ahead**

1116

1117 Here's an example of how to have an "informal subsection".

APPENDIX A

Additional material on truth isolation

yields by type	all channels	$\mu\mu$	ee	μe	$e\mu$
signal	4011	1583.2	531.7	793.1	1103.1
ww qcd	252.6	105.8	30.4	48	68.4
charge flip	2528.4	0.0	2075.4	255.1	197.8
fakes	7135.4	0.0	4675.1	1904.3	555.9
diboson	2370.4	581.2	491.8	517.9	779.6
triboson	125.5	49.1	17.8	24.6	34.1
top	90150.5	26618	15301.6	25277.9	22953.1
z+jets	241.2	0.0	0.0	0.0	241.2
w+jets	31.4	3.9	7.6	13.2	6.7
total bkg	102803.9	27354	22592	28027.8	24830.1
signal	4011	1583.2	531.7	793.1	1103.1

Table A.1: Event yields prior to applying any form of truth-based isolation criteria.

yields by type	all channels	$\mu\mu$	ee	μe	$e\mu$
signal	3470.5	1427.3	428.8	675.8	938.7
ww qcd	205.8	90.8	22.7	38.3	54
charge flip	2398.3	0.0	2104.6	95.8	197.9
fakes	4309.7	0.0	3390.6	750.8	168.3
diboson	1552.4	311.3	355.6	346.8	538.7
triboson	115	46.8	15.4	21.6	31.2
top	156.9	42.3	14.8	76.6	23.3
z+jets	0.0	0.0	0.0	0.0	0.0
w+jets	0.3	0.0	0.0	0.3	0.0
total bkg	8738.1	491.3	5903.7	1329.8	1013.4
signal	3470.5	1427.3	428.8	675.8	938.7

Table A.2: Event yields after applying a test version of the truth-based isolation.

Bibliography

- 1122 [1] ATLAS Collaboration Collaboration, *Observation of electroweak production of a same-sign W*
 1123 *boson pair in association with two jets in pp collisions at $\sqrt{s} = 13$ TeV with the ATLAS*
 1124 *detector*, Tech. Rep. ATLAS-CONF-2018-030, CERN, Geneva, Jul, 2018.
 1125 <https://cds.cern.ch/record/2629411>. (document), 5, 5.8, 6.6.2
- 1126 [2] S. L. Glashow, *The Renormalizability of Vector Meson Interactions*, Nucl. Phys. **10** (1959)
 1127 107–117. 2.2
- 1128 [3] A. Salam and J. C. Ward, *Weak and Electromagnetic Interactions*, Nuovo Cimento **11** (1959)
 1129 568–577. 2.2
- 1130 [4] L. R. Evans and P. Bryant, *LHC Machine*, JINST **3** (2008) S08001.
 1131 <https://cds.cern.ch/record/1129806>. This report is an abridged version of the LHC
 1132 Design Report (CERN-2004-003). 3.1
- 1133 [5] ATLAS Collaboration, *The ATLAS Experiment at the CERN Large Hadron Collider*, JINST
 1134 **3** (2008) S08003. 3.1
- 1135 [6] ATLAS Collaboration Collaboration, *Alignment of the ATLAS Inner Detector Tracking*
 1136 *System with 2010 LHC proton-proton collisions at $\sqrt{s} = 7$ TeV*, Tech. Rep.
 1137 ATLAS-CONF-2011-012, CERN, Geneva, Mar, 2011.
 1138 <https://cds.cern.ch/record/1334582>. 4
- 1139 [7] ATLAS Collaboration, ATLAS Collaboration, *Evidence for Electroweak Production*
 1140 *of $W^\pm W^\pm jj$ in pp Collisions at $\sqrt{s} = 8$ TeV with the ATLAS Detector*, Phys. Rev. Lett. **113**
 1141 (2014) no. 14, 141803, arXiv:1405.6241 [hep-ex]. 5
- 1142 [8] CMS Collaboration, V. Khachatryan et al., *Study of vector boson scattering and search for*
 1143 *new physics in events with two same-sign leptons and two jets*, Phys. Rev. Lett. **114** (2015)
 1144 no. 5, 051801, arXiv:1410.6315 [hep-ex]. 5
- 1145 [9] CMS Collaboration, CMS Collaboration, *Observation of electroweak production of same-sign*
 1146 *W boson pairs in the two jet and two same-sign lepton final state in proton-proton collisions*
 1147 *at $\sqrt{s} = 13$ TeV*, arXiv:1709.05822 [hep-ex]. 5
- 1148 [10] C. Bittrich, W. K. Di Clemente, E. M. Duffield, C. Geng, G. Gonella, J. Guo, B. Heinemann,
 1149 T. Herrmann, F. Iltzsche Speiser, M. Kobel, K. Koeneke, J. I. Kroll, S. Li, J. Liu, Y. Liu, J. A.

- 1150 Manjarres Ramos, G. Azuelos, C. A. Lee, M. Mittal, C. Mwewa, R. Ospanov, S. Pagan Griso,
 1151 K. J. Potamianos, M. Shapiro, P. Sommer, S. Todt, Y. Wu, W. Xu, S. Yacoob, H. Yang,
 1152 L. Zhang, Z. Zhao, B. Zhou, J. Zhu, and M.-A. Pleier, *Support note for measurement of*
 1153 *electroweak $W^\pm W^\pm jj$ production at $\sqrt{s} = 13$ TeV*, Tech. Rep. ATL-COM-PHYS-2018-252,
 1154 CERN, Geneva, Mar, 2018. <https://cds.cern.ch/record/2309552>. 5, 5.3.3
- 1155 [11] B. W. Lee, C. Quigg, and H. B. Thacker, *The Strength of Weak Interactions at Very*
 1156 *High-Energies and the Higgs Boson Mass*, Phys. Rev. Lett. **38** (1977) 883–885. 5.0.1
- 1157 [12] S. D. Rindani, *Strong gauge boson scattering at the LHC*, in *Physics at the Large Hadron*
 1158 *Collider*, A. Datta, B. Mukhopadhyaya, A. Raychaudhuri, A. K. Gupta, C. L. Khetrapal,
 1159 T. Padmanabhan, and M. Vijayan, eds., pp. 145–155. 2009. arXiv:0910.5068 [hep-ph]. 5.0.1
- 1160 [13] A. Alboteanu, W. Kilian, and J. Reuter, *Resonances and Unitarity in Weak Boson Scattering*
 1161 *at the LHC*, JHEP **11** (2008) 010, arXiv:0806.4145 [hep-ph]. 5.0.1, 5.1
- 1162 [14] ATLAS Collaboration, *Observation of a new particle in the search for the Standard Model*
 1163 *Higgs boson with the ATLAS detector at the LHC*, Phys. Lett. B **716** (2012) 1,
 1164 arXiv:1207.7214 [hep-ex]. 5.0.1
- 1165 [15] CMS Collaboration, *Observation of a new boson at a mass of 125 GeV with the CMS*
 1166 *experiment at the LHC*, Phys. Lett. B **716** (2012) 30, arXiv:1207.7235 [hep-ex]. 5.0.1
- 1167 [16] J. M. Campbell and R. K. Ellis, *Higgs Constraints from Vector Boson Fusion and Scattering*,
 1168 JHEP **04** (2015) 030, arXiv:1502.02990 [hep-ph]. 5.0.1, 5.0.2
- 1169 [17] M. SZleper, *The Higgs boson and the physics of WW scattering before and after Higgs*
 1170 *discovery*, arXiv:1412.8367 [hep-ph]. 5.0.1
- 1171 [18] E. Accomando, A. Ballestrero, A. Belhouari, and E. Maina, *Isolating Vector Boson Scattering*
 1172 *at the LHC: Gauge cancellations and the Equivalent Vector Boson Approximation vs complete*
 1173 *calculations*, Phys. Rev. **D74** (2006) 073010, arXiv:hep-ph/0608019 [hep-ph]. 5.0.1
- 1174 [19] P. Anger, B. Axen, T. Dai, C. Gumpert, C. Hasterok, B. Heinemann, M. Hurwitz, N. Ilic,
 1175 M. Kobel, J. Liu, L. Liu, J. Metcalfe, S. Pagan Griso, B. Zhou, S. Hou, M.-A. Pleier,
 1176 U. Schnoor, J. Searcy, F. Socher, A. Sood, A. Vest, L. Xu, and J. Zhu, *Same Sign $W^\pm W^\pm$*
 1177 *Production and Limits on Anomalous Quartic Gauge Couplings*, Tech. Rep.
 1178 ATL-COM-PHYS-2013-990, CERN, Geneva, Jul, 2013.
 1179 <https://cds.cern.ch/record/1561731>. Internal note for approved paper STDM-2013-06
 1180 <https://atlas.web.cern.ch/Atlas/GROUPS/PHYSICS/PAPERS/STDM-2013-06/>. 5.0.2, 5.1,
 1181 5.7
- 1182 [20] J. Almond, L. Bianchini, C. Blocker, J. Klinger, A. Maslennikov, M. Owen, K. Skovpen,
 1183 Y. Tikhonov, and U. Yang, *Search for heavy neutrino, W_R and Z_R gauge bosons in events*
 1184 *with two high- P_T leptons and jets with the ATLAS detector in pp collisions at $\sqrt{s} = 8$ TeV*,
 1185 Tech. Rep. ATL-COM-PHYS-2013-810, CERN, Geneva, Jun, 2013.
 1186 <https://cds.cern.ch/record/1555805>. This is the supporting note for EXOT-2012-24,
 1187 which is now published as JHEP07 (2015) 162. 5.0.3
- 1188 [21] ATLAS Collaboration, M. Aaboud et al., *Luminosity determination in pp collisions at $\sqrt{s} =$*
 1189 *8 TeV using the ATLAS detector at the LHC*, Eur. Phys. J. **C76** (2016) no. 12, 653,
 1190 arXiv:1608.03953 [hep-ex]. 5.1

- 1191 [22] G. Avoni et al., *The new LUCID-2 detector for luminosity measurement and monitoring in*
 1192 *ATLAS*, JINST **13** (2018) no. 07, P07017. 5.1
- 1193 [23] ATLAS Collaboration, G. Aad et al., *The ATLAS Simulation Infrastructure*, Eur. Phys. J.
 1194 **C70** (2010) 823–874, arXiv:1005.4568 [physics.ins-det]. 5.1.1
- 1195 [24] S. Agostinelli et al., *GEANT4 - a simulation toolkit*, Nucl. Instrum. Meth. **A506** (2003)
 1196 250–303. 5.1.1
- 1197 [25] T. Sjostrand, S. Mrenna, and P. Skands, *A Brief Introduction to PYTHIA 8.1*, Comput.
 1198 Phys. Commun. **178** (2008) 852–867, arXiv:0710.3820 [hep-ph]. 5.1.1
- 1199 [26] T. Gleisberg et al., *Event generation with SHERPA 1.1*, JHEP **02** (2009) 007,
 1200 arXiv:0811.4622 [hep-ph]. 5.1.1
- 1201 [27] S. Schumann and F. Krauss, *A parton shower algorithm based on Catani-Seymour dipole*
 1202 *factorization*, JHEP **03** (2008) 038, arXiv:0709.1027 [hep-ph]. 5.1.1
- 1203 [28] S. Höche, F. Krauss, S. Schumann, and F. Siegert, *QCD matrix elements and truncated*
 1204 *showers*, JHEP **05** (2009) 053, arXiv:0903.1219 [hep-ph]. 5.1.1
- 1205 [29] R. D. Ball et al., *Parton distributions for the LHC Run II*, JHEP **04** (2015) 040,
 1206 arXiv:1410.8849 [hep-ph]. 5.1.1
- 1207 [30] S. Alioli, P. Nason, C. Oleari, and E. Re, *A general framework for implementing NLO*
 1208 *calculations in shower Monte Carlo programs: the POWHEG BOX*, JHEP **06** (2010) 043,
 1209 arXiv:1002.2581 [hep-ph]. 5.1.1
- 1210 [31] A. Ballestrero et al., *Precise predictions for same-sign W-boson scattering at the LHC*, Eur.
 1211 Phys. J. **C78** (2018) no. 8, 671, arXiv:1803.07943 [hep-ph]. 5.1.1
- 1212 [32] J. Alwall, R. Frederix, S. Frixione, V. Hirschi, F. Maltoni, O. Mattelaer, H. S. Shao,
 1213 T. Stelzer, P. Torrielli, and M. Zaro, *The automated computation of tree-level and*
 1214 *next-to-leading order differential cross sections, and their matching to parton shower*
 1215 *simulations*, JHEP **07** (2014) 079, arXiv:1405.0301 [hep-ph]. 5.1.1
- 1216 [33] H.-L. Lai, M. Guzzi, J. Huston, Z. Li, P. M. Nadolsky, J. Pumplin, and C. P. Yuan, *New*
 1217 *parton distributions for collider physics*, Phys. Rev. D **82** (2010) 074024, arXiv:1007.2241
 1218 [hep-ph]. 5.1.1
- 1219 [34] T. Sjostrand, S. Mrenna, and P. Skands, *PYTHIA 6.4 physics and manual*, JHEP **05** (2006)
 1220 026, arXiv:0603175 [hep-ph]. 5.1.1
- 1221 [35] ATLAS Collaboration, G. Aad et al., *Muon reconstruction performance of the ATLAS*
 1222 *detector in protonproton collision data at $\sqrt{s} = 13$ TeV*, Eur. Phys. J. **C76** (2016) no. 5, 292,
 1223 arXiv:1603.05598 [hep-ex]. 5.2.1.1, 5
- 1224 [36] ATLAS Collaboration Collaboration, *Electron efficiency measurements with the ATLAS*
 1225 *detector using the 2015 LHC proton-proton collision data*, Tech. Rep.
 1226 ATLAS-CONF-2016-024, CERN, Geneva, Jun, 2016.
 1227 <https://cds.cern.ch/record/2157687>. 5.2.1.2
- 1228 [37] M. Cacciari, G. P. Salam, G. Soyez, *The anti- k_t jet clustering algorithm*, JHEP **04** (2008) 063,
 1229 arXiv:0802.1189 [hep-ph]. 5.2.1.3, 6.4.1

- 1230 [38] ATLAS Collaboration, M. Aaboud et al., *Jet energy scale measurements and their systematic*
 1231 *uncertainties in proton-proton collisions at $\sqrt{s} = 13$ TeV with the ATLAS detector*, Phys.
 1232 Rev. D96 (2017) no. 7, 072002, arXiv:1703.09665 [hep-ex]. 5.2.1.3
- 1233 [39] *Tagging and suppression of pileup jets with the ATLAS detector*, Tech. Rep.
 1234 ATLAS-CONF-2014-018, CERN, Geneva, May, 2014.
 1235 <http://cds.cern.ch/record/1700870>. 5.2.1.3
- 1236 [40] D. Adams, C. Anastopoulos, A. Andreatta, M. Aoki, L. Asquith, M. Begel, F. Bernlochner,
 1237 U. Blumenschein, A. Bocci, S. Cheatham, W. Davey, P.-A. Delsart, P.-O. DeViveiros,
 1238 A. Dewhurst, D. Duschinger, F. Filthaut, P. Francavilla, F. Garberson, S. Head, A. Henrichs,
 1239 A. Hoecker, M. Kagan, B. Kersevan, T. Khoo, B. Lenzi, D. Lopez Mateos, B. Malaescu,
 1240 Z. Marshall, T. Martin, C. Meyer, A. Morley, W. Murray, M. zur Nedden, R. Nicolaïdou,
 1241 S. Pagan Griso, G. Pasztor, P. Petroff, C. Pizio, R. Polifka, X. Poveda, R. Reece, F. Ruehr,
 1242 F. Salvatore, R. Sandstroem, T. Scanlon, D. Scheirich, S. Schramm, A. Schwartzman,
 1243 K. Suruliz, M. Sutton, E. Thompson, M. Tripiana, A. Tuna, S. Viel, M. Vincter, I. Vivarelli,
 1244 M. Wielers, A. Wildauer, and Z. Zinonos, *Recommendations of the Physics Objects and*
 1245 *Analysis Harmonisation Study Groups 2014*, Tech. Rep. ATL-PHYS-INT-2014-018, CERN,
 1246 Geneva, Jul, 2014. <https://cds.cern.ch/record/1743654>. 5.2.1.4
- 1247 [41] ATLAS Collaboration, M. Aaboud et al., *Measurement of the cross-section for producing a W*
 1248 *boson in association with a single top quark in pp collisions at $\sqrt{s} = 13$ TeV with ATLAS*,
 1249 JHEP 01 (2018) 063, arXiv:1612.07231 [hep-ex]. 5.2.1.4
- 1250 [42] ATLAS Collaboration, M. Aaboud et al., *Performance of missing transverse momentum*
 1251 *reconstruction with the ATLAS detector using proton-proton collisions at $\sqrt{s} = 13$ TeV*, Eur.
 1252 Phys. J. C78 (2018) no. 11, 903, arXiv:1802.08168 [hep-ex]. 5.2.2
- 1253 [43] ATLAS Collaboration, M. Aaboud et al., *Measurements of b -jet tagging efficiency with the*
 1254 *ATLAS detector using $t\bar{t}$ events at $\sqrt{s} = 13$ TeV*, JHEP 08 (2018) 089, arXiv:1805.01845
 1255 [hep-ex]. 5.2.2
- 1256 [44] J.-F. Arguin, J. Claude, G. Gonella, B. P. Kersevan, and K tech. rep. 5.3.3
- 1257 [45] R. Steerenberg, *LHC Report: Another run is over and LS2 has just begun...*,
 1258 <https://home.cern/news/news/accelerators/lhc-report-another-run-over-and-ls2-has-just-begun>, 2018. Accessed: 2018-12-14. 6
- 1259
- 1260 [46] *Letter of Intent for the Phase-I Upgrade of the ATLAS Experiment*, Tech. Rep.
 1261 CERN-LHCC-2011-012. LHCC-I-020, CERN, Geneva, Nov, 2011.
 1262 <http://cds.cern.ch/record/1402470>. 6
- 1263 [47] G. Apollinari, I. Bjar Alonso, O. Brning, M. Lamont, and L. Rossi, *High-Luminosity Large*
 1264 *Hadron Collider (HL-LHC): Preliminary Design Report*. CERN Yellow Reports: Monographs.
 1265 CERN, Geneva, 2015. <https://cds.cern.ch/record/2116337>. 6
- 1266 [48] ATLAS Collaboration Collaboration, ATLAS Collaboration, *ATLAS Phase-II Upgrade*
 1267 *Scoping Document*, Cern-lhcc-2015-020, Geneva, Sep, 2015.
 1268 <http://cds.cern.ch/record/2055248>. 6
- 1269 [49] D. Espriu and B. Yencho, *Longitudinal WW scattering in light of the “Higgs boson”*
 1270 *discovery*, Phys. Rev. D 87 (2013) 055017, arXiv:1212.4158 [hep-ph]. 6, 6.1

- 1271 [50] ATLAS Collaboration Collaboration, *Prospects for the measurement of the $W^\pm W^\pm$ scattering*
1272 *cross section and extraction of the longitudinal scattering component in pp collisions at the*
1273 *High-Luminosity LHC with the ATLAS experiment*, Tech. Rep. ATL-PHYS-PUB-2018-052,
1274 CERN, Geneva, Dec, 2018. <http://cds.cern.ch/record/2652447>. 6
- 1275 [51] ATLAS Collaboration Collaboration, *Studies on the impact of an extended Inner Detector*
1276 *tracker and a forward muon tagger on $W^\pm W^\pm$ scattering in pp collisions at the*
1277 *High-Luminosity LHC with the ATLAS experiment*, Tech. Rep. ATL-PHYS-PUB-2017-023,
1278 CERN, Geneva, Dec, 2017. <https://cds.cern.ch/record/2298958>. 6
- 1279 [52] T. Sjöstrand, S. Ask, J. R. Christiansen, R. Corke, N. Desai, P. Ilten, S. Mrenna, S. Prestel,
1280 C. O. Rasmussen, and P. Z. Skands, *An Introduction to PYTHIA 8.2*, *Comput. Phys.*
1281 *Commun.* **191** (2015) 159–177, <arXiv:1410.3012> [hep-ph]. 6.2
- 1282 [53] ATLAS Collaboration Collaboration, *Expected performance for an upgraded ATLAS detector*
1283 *at High-Luminosity LHC*, Tech. Rep. ATL-PHYS-PUB-2016-026, CERN, Geneva, Oct, 2016.
1284 <http://cds.cern.ch/record/2223839>. 6.3
- 1285 [54] P. C. Bhat, H. B. Prosper, S. Sekmen, and C. Stewart, *Optimizing Event Selection with the*
1286 *Random Grid Search*, *Comput. Phys. Commun.* **228** (2018) 245–257, <arXiv:1706.09907>
1287 [hep-ph]. 6.5.1
- 1288 [55] G. Cowan, K. Cranmer, E. Gross, and O. Vitells, *Asymptotic formulae for likelihood-based*
1289 *tests of new physics*, *Eur. Phys. J.* **C71** (2011) 1554, <arXiv:1007.1727> [physics.data-an].
1290 [Erratum: *Eur. Phys. J.* C73, 2501(2013)]. 6.5.1